The Astrophysical Journal, 702:506–522, 2009 September 1 doi:10.1088/0004-637X/702/1/506

THE CLOWES–CAMPUSANO LARGE QUASAR GROUP SURVEY. I. *GALEX* SELECTED SAMPLE OF LYMAN BREAK GALAXIES AT $z \sim 1$

L. Haberzettl[1], G. M. Williger[1,2,3], J. T. Lauroesch[1], C. P. Haines[4], D. Valls-Gabaud[5], K. A. Harris[6], A. M. Koekemoer[7], J. Loveday[8], L. E. Campusano[9], R. G. Clowes[6], R. Davé[10], M. J. Graham[11], and I. K. Söchting[12]
[1] Department of Physics and Astronomy, University of Louisville, Louisville, KY 40292, USA; lghabe01@louisville.edu
[2] Department of Physics and Astronomy, Johns Hopkins University, Baltimore, MD 21218, USA
[3] Department of Physics, Catholic University of America, Washington DC 20064, USA
[4] School of Physics and Astronomy, University of Birmingham, Edgbaston, Birmingham, B15 2TT, UK
[5] GEPI, CNRS UMR 8111, Observatoire de Paris, 5 Place Jules Janssen, 92195 Meudon Cedex, France
[6] Institute for Astrophysics, University of Central Lancashire, Preston PR1 2HE, UK
[7] Space Telescope Science Institute, 3700 San Martin Drive, Baltimore, MD 21218, USA
[8] Astronomy Centre, University of Sussex, Falmer, Brighton BN1 9QH, UK
[9] Departamento de Astronomía, Universidad de Chile, Casilla 36-D, Santiago, Chile
[10] Department of Astronomy, University of Arizona, 933N Cherry Ave., Tucson, AZ 85721, USA
[11] CACR, California Institute of Technology, Pasadena, CA 91125, USA
[12] University of Oxford, Astrophysics, Denys Wilkinson Building, Keble Road, Oxford OX1 3RH, UK
Received 2008 October 23; accepted 2009 June 23; published 2009 August 13

ABSTRACT

The nature of galaxy structures on large scales is a key observational prediction for current models of galaxy formation. The Sloan Digital Sky Survey (SDSS) and the 2dF galaxy survey have revealed a number of structures on 40–150 h^{-1} Mpc scales at low redshifts, and some even larger ones. To constrain galaxy number densities, luminosities, and stellar populations in large structures at higher redshift, we have investigated two sheet-like structures of galaxies at $z = 0.8$ and 1.3 spanning 150 h^{-1} comoving Mpc embedded in large quasar groups (LQGs) extending over at least 200 h^{-1} Mpc. We present first results of an analysis of these sheet-like structures using two contiguous 1 deg *Galaxy Evolution Explorer* (*GALEX*) fields (FUV and NUV) cross-correlated with optical data from the SDSS. We derive a sample of 462 Lyman break galaxy (LBG) candidates coincident with the sheets. Using the *GALEX* and SDSS data, we show that the overall average spectral energy distribution of a LBG galaxy at $z \sim 1$ is flat (in f_λ) in the rest-frame wavelength range from 1500 Å to 4000 Å, implying evolved populations of stars in the LBGs. From the luminosity functions we get indications for overdensities in the two LQGs compared to their foreground regions. Similar conclusions come from the calculation of the 2-point correlation function, showing a 2σ overdensity for the LBGs in the $z \sim 0.8$ LQG on scales of 1.6 to 4.8 Mpc, indicating similar correlation scales for our LBG sample as their $z \sim 3$ counterparts.

Key words: galaxies: distances and redshifts – galaxies: evolution – large-scale structure of universe – quasars: general

Online-only material: color figures, extended figures, machine-readable table

1. INTRODUCTION

The relation between galaxy populations, environment, and the quasar/active galactic nucleus (AGN) phase of galaxy evolution is crucial for a complete picture of galaxy and structure formation. Galaxy redshift surveys have revealed the cosmic web, a cellular distribution (e.g., Doroshkevich & Dubrovich 2001) on scales of 40–150 h^{-1} Mpc or more. In particular, large structures were found in the SDSS and 2dF redshift survey (Adelman-McCarthy et al. 2006; Croom et al. 2004), tracing galaxy populations and star formation in the cosmic web. The ΛCDM model predicts weakly nonlinear structures of these dimensions at low redshift, but simulations (e.g., Evrard et al. 2002) indicate that "Great Wall"-like sheets become rare at $z \sim 1$. Clearly the detection of very large filaments and the presence of a large number of high-redshift clusters are an interesting test of current cosmologies. Distinct blue and red galaxy sequences at $0 < z < 0.7$ indicate significant environmental effects on the red fraction at fixed luminosity (e.g., Balogh et al. 2004; Cassata et al. 2007). Environmental effects are especially key in triggering/quenching star formation through mergers, harassment, and gas stripping (Postman et al. 2005), though on cluster outskirts, some star formation also goes on (Duc et al. 2002; Coia et al. 2005). There is clear evidence that galaxies in filaments falling into clusters of galaxies undergo bursts of star formation prior to reaching the cluster, both at low redshifts (Porter et al. 2008) and at $z \sim 1$ (Koyama et al. 2008) even though the specific star formation rates (SFRs) may be lower for those galaxies in the red sequence (e.g., Nakata et al. 2002). Understanding these mechanisms is essential to assess the role of environment in galaxy evolution.

Extremely dense regions should show the most extreme environmental effects. The epoch $z \sim 1$ is a key point, where the galaxy luminosity function (LF) still can be readily probed to faint levels and environmental effects appear to affect galaxy evolution strongly. Recent work (Gerke et al. 2007; Noeske et al. 2007) indicates that $z \sim 1$–1.5 is where the galaxy color–density relation establishes itself: at lower z red galaxies prefer dense environments, while at earlier times star-forming and passive galaxies inhabit similar environments, with possible evidence for an inversion (Cooper et al. 2007, 2008; Elbaz et al. 2007). However, Quadri et al. (2007) find that the color–density relation (in the sense of redder galaxies being located in denser environments) extends to redshifts $z > 2$. Hence studies of

galaxies in overdense environments at this epoch promise to yield crucial insights into this critical part of galaxy formation theory.

Quasars may signal gas-rich merger environments (Hopkins et al. 2008), and large quasar groups (LQGs) are potentially unique structure markers on scales up to hundreds of Mpc. LQGs could therefore provide a very efficient means to study both quasars and galaxies in a wide variety of environments, from low to high densities. Analogous to star formation quenching (e.g., Coia et al. 2005), quasars form preferentially in cluster outskirts at $z \sim 0.4$, and delineate the underlying large-scale structure (LSS; e.g., Söchting et al. 2002, 2004). Although LQGs are too large to be virialized at their redshifts, they are still highly biased tracers of what may be the largest scale density perturbations. The average LQG space density is 7 Gpc^{-3} at $0.3 < z < 1.9$ (Pilipenko 2007), or ∼3–4× below supercluster number densities at $z < 0.1$ (∼25 Gpc^{-3}; Swinbank et al. 2007). They form two classes, ∼70% with 6–8 members, average sizes of 90 h^{-1} Mpc, and overdensities of ∼10, and ∼30% with 15–19 member, average scales of 200 h^{-1} Mpc and overdensities of 4. Six such mega-structures were found by Pilipenko (2007) in the 2dF quasar survey (750 deg^2), implying 500–1000 "jumbo" LQGs in the sky.

One aspect to understanding the formation of LSS is the star formation within them and its connection to the environment. Lyman break galaxies (LBGs; Steidel et al. 1996) are one representative class of galaxies for ongoing star formation, forming stars on relative high levels (Madau et al. 1998). The Lyman break at 912 Å (rest frame) is a spectral signature which makes it relatively easy to detect large numbers of LBGs at high redshifts ($z > 2$) by color selection, using the dropout technique (Steidel et al. 1995). Therefore LBGs were one of the first confirmed population of high-redshift galaxies (Steidel et al. 1995). They were found to be more metal rich than expected, with metallicities $Z > 0.1\ Z_\odot$ (Teplitz et al. 2000; Pettini et al. 2001). Their stellar populations are similar to those found in local starburst galaxies with stellar masses of several $10^9\ M_\odot$ up to $10^{10}\ M_\odot$ for L^* luminous LBGs (Papovich et al. 2001). Therefore, they show only 0.1 times the mass of present day L^* galaxies. LBGs at $z > 2$ are expected to be the precursors for the present day massive galaxies evolving via mergers into massive elliptical galaxies at $z = 0$ (Nagamine 2002). However, the $z \sim 1$ LBGs are likely to be the progenitors of rather less massive ellipticals, 0.1–1 L^*, since there is only little growth in the elliptical galaxy population after $z \sim 1$. Although the bulk of the ongoing star formation at $2 \leqslant z \leqslant 4$ can be observed in the optical wavelength range, dust plays a substantial role in high-redshift galaxy evolution. In contrast to early assumptions as by Madau et al. (1998), studies of the dust attenuation of Vijh et al. (2003) showed that LBGs are affected by extinction up to ∼5 mag (rest frame 1600 Å), requiring significant corrections to SFRs from LBGs.

Other types of galaxies such as luminous and ultraluminous infrared galaxies (LIRGS and ULIRGS) require identification in the mid-IR. In those wavebands the observing capabilities (e.g., *Spitzer*) mostly do not allow coverage of large areas with high spatial resolution down to low sensitivities. LBGs are easier to survey and therefore offer an efficient statistical measure of star formation in the early universe, as long as results are interpreted with attention to extinction from dust.

LBGs reflect value as mass tracers by virtue of their correlation properties. At $z \gtrsim 2$ LBGs show strong clustering with power-law slopes of the angular correlation function of $\beta \sim 0.5$–0.8 on scales of 30″–100″ (Porciani & Giavalisco 2002; Foucaud et al. 2003; Hildebrandt et al. 2007), with brighter LBGs clustering more strongly. Their correlation lengths are ∼4–6 h^{-1} Mpc. A similar correlation length range was observed between AGNs and LBGs at $z \sim 3$ (Adelberger & Steidel 2005), for AGN black hole masses of $5.8 < \log(M_{BH}/M_\odot) < 10.5$.

Although we have very good knowledge about LBGs at $z \gtrsim 2$, we are only now observing $z \sim 1$ LBGs in large numbers. First results for LBGs at this critical epoch of galaxy evolution were published by Burgarella et al. (2006, 2007) using CDF-South data. They defined their sample of $z \sim 1$ LBGs using *Galaxy Evolution Explorer* (*GALEX*) observations combined with multiwavelength coverage from X-ray to mid-IR. The majority of their LBG sample consists of disk-dominated galaxies with a small number (∼20%) of interacting/merging members and almost no spheroidals. They found that UV-luminous LBGs are less affected by dust than UV-faint ones. Burgarella et al. (2007) also showed from comparison to model spectral energy distributions (SEDs) that the averaged spectra of LBGs indicate luminosity-weighted (SEDs which are dominated by the brightest stars in the galaxy) ages between 250 and 500 Myr. LBGs at $z \sim 1$ therefore are an important contributor to the UV luminosity density and represent the majority of star formation, as disk and irregular galaxies identified in the LBG sample of Burgarella et al. (2006, 2007) should represent the majority of the star formation at $z \sim 1$ based on UV to mid-IR SEDs from GEMS (Wolf et al. 2005; Bell et al. 2005).

In contrast to Burgarella et al., we report first results from a study of star-forming galaxies at $z \sim 1$ in regions with high quasar overdensities, as opposed to the presumed typical CDF-S. The high quasar space density enables us to make a comparison to the higher redshift LBG–AGN correlation of Adelberger & Steidel (2005). We describe our data and selection method in Section 2 followed by a description of our photo-z determinations in Section 3. Results from the analysis of the stacked SEDs of subsamples of our LBGs in different redshift intervals are presented in Sections 4 and 5, followed by summaries and conclusions in Section 6. Our sample increases the number of published LBG galaxies at $z \sim 1$ by about a factor of 2. Throughout the paper we use a cosmology with $H_0 = 71$ km s^{-1} Mpc^{-1}, $\Omega_M = 0.3$, and $\Omega_\Lambda = 0.7$. All distances quoted are comoving distances, unless otherwise stated.

2. OBSERVATIONS

2.1. Target Field

We observed part of the Clowes–Campusano LQG (CCLQG), which is the largest known LQG and has the most members. It contains at least 18 bright quasars at $1.2 < z < 1.5$ and a spatial overdensity of 3 for $B_J \leqslant 20.0$ mag (Clowes & Campusano 1991, 1994; Graham et al. 1995; Clowes et al. 1999; Schneider et al. 2007). The CCLQG covers ∼2.5 deg × 5 deg (∼120 × 240 h^{-2} Mpc^2) and is 590 h^{-1} Mpc deep. It was discovered in a ∼25.3 deg^2 objective-prism survey using UK Schmidt plate data (plate UJ5846P or ESO/SERC field 927; Clowes & Campusano 1991) and represents one of the largest known structures at $z > 1$. It is 3× denser in bright ($M_I < -25$) quasars compared to the DEEP2 fields (Figure 1). Previous studies of the CCLQG showed an associated factor 3 overdensity of Mg II absorbers at $1.2 < z < 1.5$ (Williger et al. 2002), which are linked to luminous galaxies (e.g., Steidel et al. 1997; Guillemin & Bergeron 1997). There is also a foreground

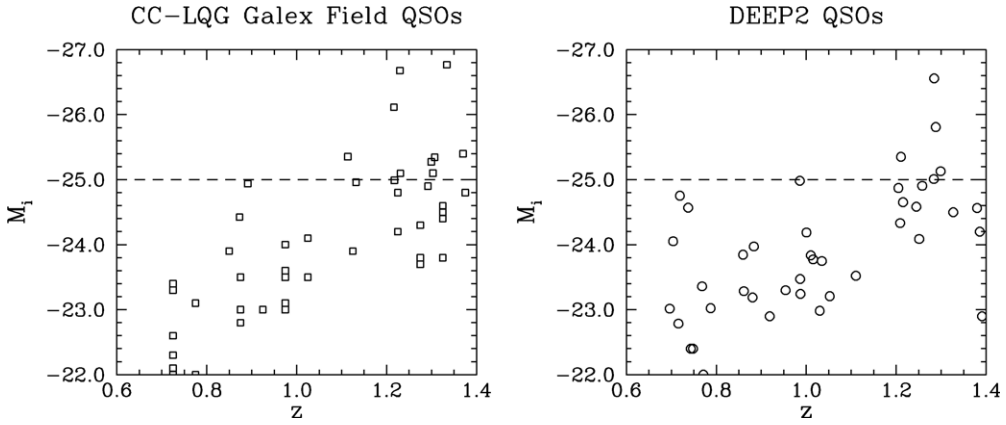

Figure 1. Distribution of QSO and AGN M_I magnitudes vs. z for our two *GALEX* fields (left, 2.2 deg^2) and the four DEEP2 fields (right, 3 deg^2; Coil et al. 2007). The QSO redshifts for the *GALEX* fields are from Clowes & Campusano (1991, 1994) and Newman (1999). Note that this plot does not include the objects from the photometric selected catalog of Richards et al. (2007), which includes another ∼40 QSO and AGN candidates to $g \sim 22.0$ in the *GALEX* fields.

Table 1
Observation Summary

Field ID	FUV		NUV		Note
	T_{exp} (s)	m_{lim} (mag)	T_{exp} (s)	m_{lim} (mag)	
(1)	(2)	(3)	(4)	(5)	(6)
21240-GI1_035001_J104802p052610	22902	24	38624	24.0	Northern *GALEX* field
21241-GI1_035002_J105002p042644	20817	24	33021	24.0	Southern *GALEX* field

Notes. The total magnitudes in Columns 3 and 5 are the 80% completeness limits.

$z \sim 0.8$ LQG containing $\geqslant$14 quasars and spanning $3.^\circ5 \times 3^\circ$ on the sky. Studies of the galaxy populations in the LQGs showed ∼30% overdensities of red galaxies ($I - K > 3.4$) at $z = 0.8$ and $z = 1.2$ (Haines et al. 2001, 2004). The galaxy colors are consistent with an evolved population, and form sheets which span a $\sim 40' \times 34'$ subfield which we imaged deeply in VI using the CTIO Blanco 4m telescope (Haines et al. 2001, 2004). Smaller $5' \times 5'$ SOFI subfields of near-IR imaging reveal three clusters at $z \sim 0.8$ and a pair of merging clusters at $z = 1.2$ associated with a CCLQG member quasar (Haines et al. 2004).

2.2. Data

For this study we have imaged two slightly overlapping 1.2 deg fields within the CCLQG in the far-UV (FUV; $\lambda_{eff} = 1538.6$ Å) and near-UV (NUV; $\lambda_{eff} = 2315.7$ Å) filter bands, using the UV satellite *GALEX* (Galaxy Evolution Explorer). The observations were part of the Guest Investigator program, cycle 1 proposal 35. The data used in this work consist of two ∼20,000 s exposures in the FUV and two ∼35,000 s exposures in the NUV filter band (Table 1). The pipeline reduction was done by the *GALEX* team, including the photometric calibration. We are able to detect point sources with SExtractor v.2.5.0 (Bertin & Arnouts 1996) to $m_{NUV,FUV}$ ∼25.5 mag. For further analysis we used the MAG_ISO parameter as measured by SExtractor, which gives total magnitude for the measured objects. For details, see the SExtractor manual.[13] A detailed description of the completeness analysis of the data can be found in Section 2.4. Optical complementary data are from the Sloan Digital Sky Survey DR5 (June 2006; Adelman-McCarthy et al. 2007), which is sensitive to limiting magnitudes of $u = 22.0$, $g = 22.2$, $r = 22.2$, $i = 21.3$, $z = 20.5$. With the SDSS data, we have seven-band photometric information available for most of our UV-selected sample (see Section 2.3). From the SDSS we obtained model magnitudes in the five filter bands, flux values, and spectroscopic and photometric redshift information. Since confusion of sources represents a significant effect in the *GALEX* data, we chose from the SDSS list the nearest primary object (as defined by the SDSS) within 4.″5 to match our UV detections.

2.3. Sample Selection

The analysis described in the following parts of the paper is based on a sample selected in the two UV filter bands of the *GALEX* data. The source catalog has been created using SExtractor v.2.5.0. The complete catalog consists of 15,688 sources applying a detection threshold of 3.0σ and an analysis threshold of 1.5σ, using the default convolution filter of SExtractor. Additionally, we also used weight maps as well as flag images to exclude bad regions at the edge of the *GALEX* images and saturated sources within our SExtractor search. The weight maps and flag images were constructed using WEIGHT WATCHER VERSION 1.7 (Marmo & Bertin 2008). A cross-correlation with the SDSS DR5 resulted in 14,316 sources (matching radius: 4.″5). To clean our sample from false detections (e.g., bright star contaminations, reflections) we only selected objects which have a SExtractor extraction $FLAGS \leqslant 2$ in the NUV filter, which resulted in a subsample of 13,760 objects (final UV selected sample). For the star-galaxy discrimination in the sample we use the *PhotoType values* of the SDSS DR5, which works on the 95% level for objects with $r \leqslant 22.2$ mag (Adelman-McCarthy et al. 2007). We selected all objects which were marked as *GALAXY* in the SDSS data, yielding 10,982 galaxies. However, since the point-spread function (PSF) of the *GALEX* data is relatively poor (∼ 4.″5 for the FUV and ∼ 6″ for the NUV filter), it is

[13] http://terapix.iap.fr/rubrique.php?id_rubrique=91

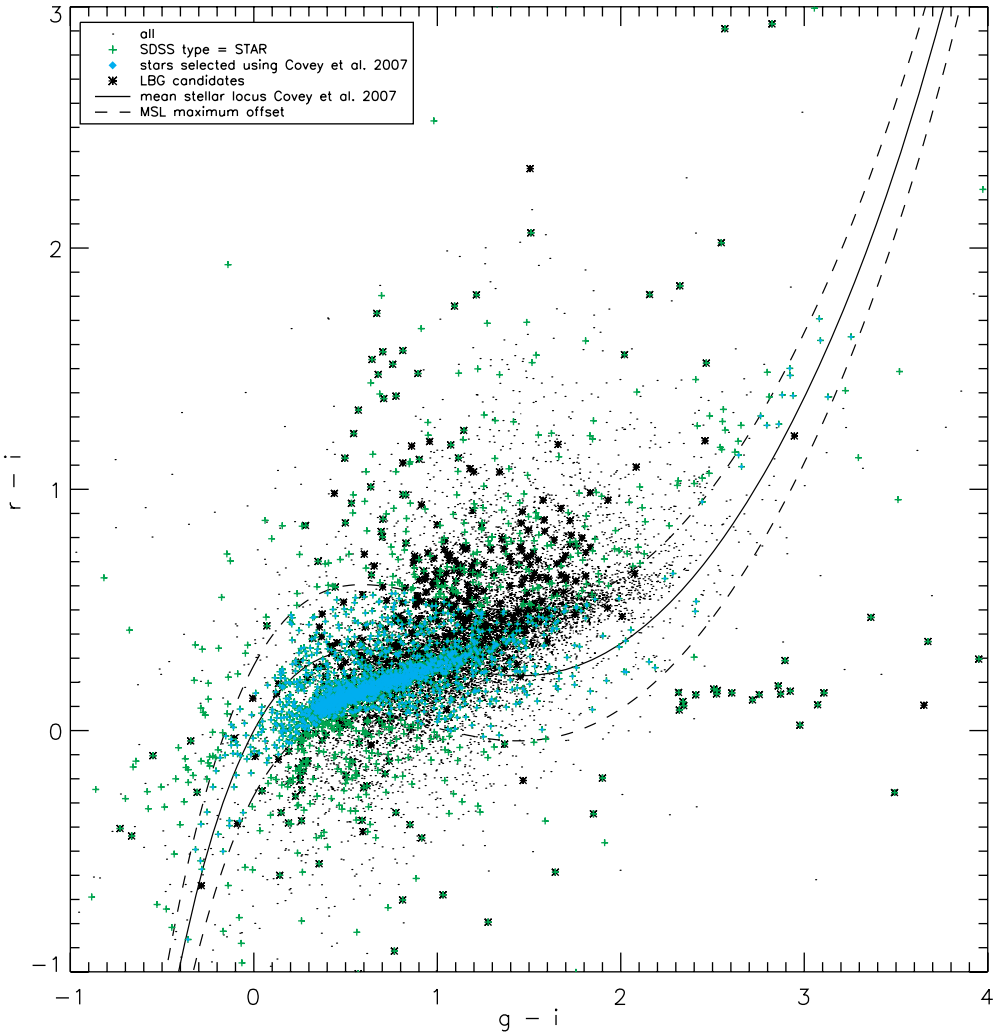

Figure 2. Color–color diagram showing the location of the MSL (red solid line) as defined by Covey et al. (2007). The blue dashed lines show the maximum offset to the analytical solution. Point sources within the maximum offset to the MSL are considered stars (cyan dots, making the streak below the MSL). Point sources outside the maximum offset to the MSL are selected as galaxy candidates (green dots). The red stars indicate the location of our LBG candidate sample.

(A color version of this figure is available in the online journal.)

difficult to distinguish between real point sources (e.g., stars or quasars) and higher redshift extended sources which are point-like in the *GALEX* beam. Therefore, to reduce the contamination of our LBG sample with faint stars, we followed our more conservative approach. To account for smaller point-like objects we also selected all objects which are marked as *STAR* and are located outside the mean stellar locus (MSL) as defined by Covey et al. (2007). For this selection we used the analytic fit for the MSL of Covey et al. (2007) in the $g - i$ versus $r - i$ color–color space (see Figure 2) and included all objects in our sample which have an offset to the MSL larger than the maximum offset indicated by the blue dashed lines. With these additional selection criteria, we ended up with a final sample of 11,635 galaxy candidates with a photometric redshift distribution as shown in Figure 6 (red bars).

To identify $z \sim 0.5$–1 LBGs, we applied a FUV dropout technique, using the selection criteria of Burgarella et al. (2006) and including only objects classified as *GALAXY* by the SDSS DR5 or outside the MSL and with $m_{\rm NUV} < 23.5$ mag and $m_{\rm FUV} - m_{\rm NUV} > 2$ mag. This resulted in a final sample of 1263 LBG galaxy candidates (618 deg^{-2}), which is only about half the detection rate of Burgarella et al., who found 1180 LBG candidates per deg^2 in the CDF-S. Without these additional selection parameters our selection would have resulted in a sample of 2566 LBG candidates or 1256 deg^{-2}, which is comparable to the results of Burgarella et al. However, unlike Burgarella et al., we only have seven-band *GALEX*+SDSS photometry as opposed to their much wider UV to mid-IR wavelength coverage and higher resolution imagery. Therefore, to reduce the contamination of our LBG sample with faint stars, we followed our more conservative approach.

2.4. Completeness and Confusion

We used a Monte Carlo-like approach to check the completeness of galaxy counts in the FUV and NUV filter bands. The process relies on a well known artificial sample of galaxies. To keep the basic image information (e.g., noise pattern, pixel size, PSF) of the original data, we simulated the artificial galaxy sample as follows. We first removed all sources detected by SExtractor from the images, to get a source-free image with the real observed background. This was done using the SExtractor check-image (*CHECKIMAGE_TYPE* = *-OBJECTS*). In the cleaned images we then placed a list of simulated galaxies constructed by running the *IRAF* task *gallist*. We created a list of 2000 synthesized galaxies randomly placed in a ∼0.7 deg^2 field.

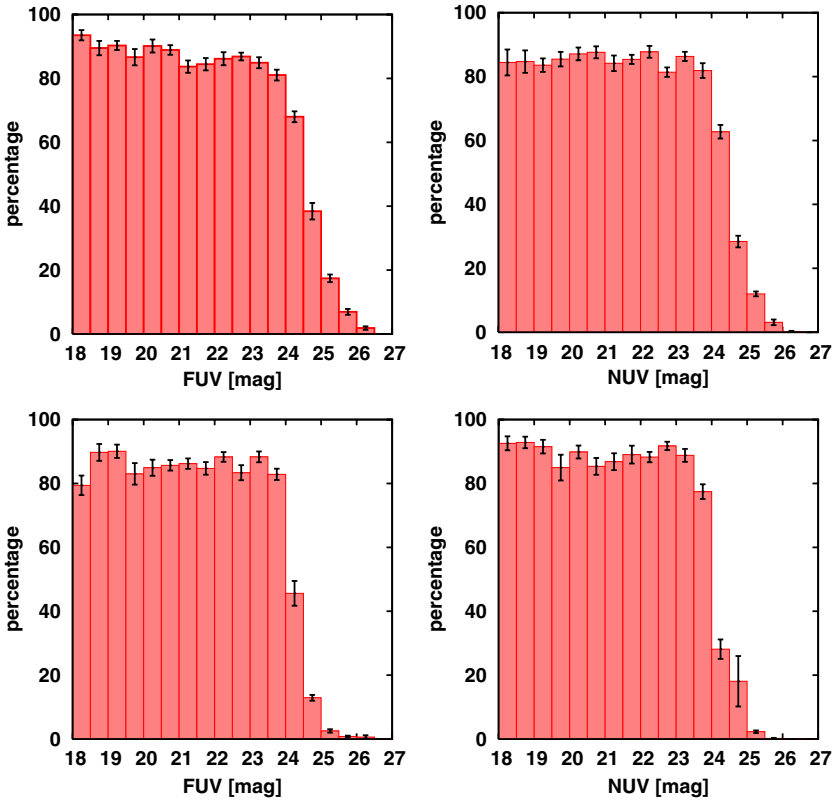

Figure 3. Results of the completeness simulations for the northern (upper row) and southern field (lower row) in the FUV (left column) and NUV (right column) filters. The marginally low values for the detection efficiency at AB < 24.0 can be explained by confusion due to the large *GALEX* PSF.
(A color version of this figure is available in the online journal.)

To simulate the artificial galaxy sample, we chose a luminosity distribution based on a power law with an exponent of 0.1. The simulated galaxy list consists of objects with total magnitudes between 14 and 25.5 mag and redshifts out to $z = 1.3$. To create the galaxies in the source-free *GALEX* images, we applied the *IRAF* task *mkobjects*. This procedure resulted in a well defined data set with a known galaxy sample which we could use for further analysis. We then photometrically analyzed the artificial galaxies and derived their total magnitudes using the galaxy fitting routine *galfit* (Peng et al. 2002) on the simulated data. In the final step, we searched the images for galaxies with SExtractor by applying the same extraction parameters as for our science data (see Section 2.3), and compared the resulting list with the input list to compute detection efficiencies. We repeated this procedure ten times and calculated the mean and standard deviation for the detection efficiencies (see Figure 3). For all four cases (FUV, NUV data for the northern and southern fields) our detection efficiency is around 80%–90% for objects with total magnitudes down to 24 AB. The detection efficiency decreases to ∼60% at 24.5 ABmag for the northern FUV and NUV images and 45%–30% for the southern images. For objects with total magnitudes fainter 24.5, the detection efficiency drops below 40% for the northern and below 20% for the southern field. The marginally low efficiencies (only 80%–90%) for the bins brighter than 24 AB can be explained by blending effects due to confusion resulting from the large pixel size of *GALEX* (1.″5) and the large PSF in the FUV (∼5″) and NUV filters (∼ 6.″7).

We therefore checked the *GALEX* detections for multiple counterparts using higher resolution optical images obtained at the CFHT with Megacam. The images reach limiting magnitudes of $r = 27$ and $z = 25$, with a mean image quality of ∼1 arcsec in both filters (for more details, see L. Haberzettl et al. 2009b, in preparation). Confusion can effect the photometry either by increasing the flux of detected objects directly or by changing the background estimates in the surrounding of the detected objects if the background is estimated locally. Since we derive a global estimate of the background within SExtractor by using a mesh size of 64 pixels (significantly larger than the PSF), this effect should be small and can be neglected. More important is the change in photometry from additional objects within one FWHM. We therefore matched all sources in the NUV, r, and z bands using a radius of 3″, which covers a slightly larger area than the 5.″4 FWHM of the *GALEX* NUV data. Our analysis show that 19% of the complete sample has two or more counterparts to $r \sim 27$. Restricting our study to counterparts with $r \leqslant 24.5$, the multiple counterpart fraction decreases to 16%. For the LBG candidates with NUV $\leqslant 23.5$, we found two or more counterparts for 22% of the sample ($r \leqslant 24$). Although these values for confusion are slightly higher then previously reported (e.g., 13%; Bianchi et al. 2007), we do not correct our sample using deconvolution methods, since our results are based on averages over samples of galaxies. The effects of confusion will be minor, compared to the scatter in our SEDs (details in Sections 4 and 5). To this point, we did not restrict optical counterpart colors. If we restrict optical counterparts to $r - z \leqslant 0.5$ (or $f_z \geqslant 1.5\, f_r$) which means the objects are likely to be either relatively old ($\gtrsim$5 Gyr) or dust reddened and in both cases have significantly reduced UV-fluxes, the fraction with $\geqslant$2 counterparts reduces to 16% for the complete sample (NUV $\leqslant 23.5$) and 10% for the LBG subsample.

Additional information about confusion results from the number of sources per beam (beams per source). We followed

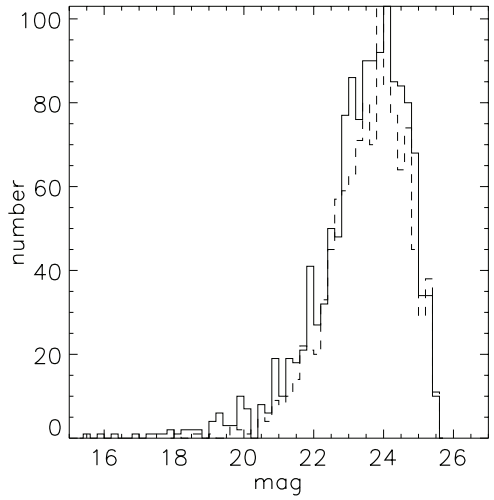

Figure 4. Comparison of the distribution in magnitudes for real (dashed) and simulated (solid) NUV *GALEX* data. The distributions are consistent with each other. Poisson errors in the real data are omitted for clarity. See text for simulation details.

the approach by Hogg (2001) as used by Burgarella et al. (2007). Restricting the galaxy sample to NUV $\leqslant 23.5$ results in $(\mathrm{s/b})^{3\sigma}_{\mathrm{conf}} = 0.0038$ sources per beam (265 beams per source). This is much shallower than the 3σ confusion limit of $(\mathrm{s/b})^{3\sigma}_{\mathrm{conf}} = 0.063$ or 16 beams per source reported by Burgarella et al. (2007) indicating that confusion will not effect our results significantly:

$$(s/b)^{3\sigma}_{\mathrm{conf}} = \frac{N_{\mathrm{sources}}}{\Omega_{GALEX}/\Omega_{\mathrm{beam}}}. \quad (1)$$

To test the effect of confusion on our photometry, we simulated *GALEX* NUV images using SkyMaker 3.1.0[14] and STUFF 1.17[15] developed by E. Bertin & P. Fouqué (http://terapix.iap.fr). The galaxy distribution was created using STUFF 1.17 default parameters for a 1024 × 1024 image and represent the galaxy sample of interest for which we wish to measure the photometry. The instrument specific parameters (e.g., pixel size, mirror size) were set to *GALEX* specifications. The galaxy distribution includes objects with $18 \leqslant \mathrm{MAG\_LIMITS} \leqslant 26.5$. We then created a simulated image with SkyMaker for a ∼33 ks exposure using the *GALEX* NUV PSF. The comparison in number density and brightness distribution between the real and the simulated *GALEX* NUV data shows good agreement (Figure 4). We added a uniformly distributed sample of 100,000 artificial background galaxies to the data, simulated using *IRAF* tasks *gallist* and *mkobjects*. The sample was made using a power-law distribution $dN \sim m^{-\beta}$ with $\beta = 0.6$, restricted to $18 \leqslant m \leqslant 28.5$ including background galaxies down to the 1% flux level of NUV magnitude limit. Comparison of SExtractor catalogs with and without the synthetic galaxies shows no significant effects on the photometric results for objects with $m \leqslant 23.5$ (see Figure 5). The rms for the change in m_{iso} is $dm_{\mathrm{rms}} = 0.0707$ mag, including objects which have $dm < 0$ resulting from changes in the deblending during the SExtractor search and/or overall higher background level due to the high number of background galaxies. The rms of change in m_{iso} accounting only for objects with $dm \geqslant 0$ is $dm_{\mathrm{rms}} = 0.0784$. This is small compared to the NUV scatter in the averaged SEDs, which can be as high as 1.5 mag. We conclude that our catalogs are 80%–90% complete down to $m_{\mathrm{NUV}} = 24$ AB. For LBG candidates we are 40%–60% complete to $\mathrm{AB}_{\mathrm{NUV}} = 24.5$.

[14] http://terapix.iap.fr/rubrique.php?id_rubrique=221
[15] http://terapix.iap.fr/rubrique.php?id_rubrique=248

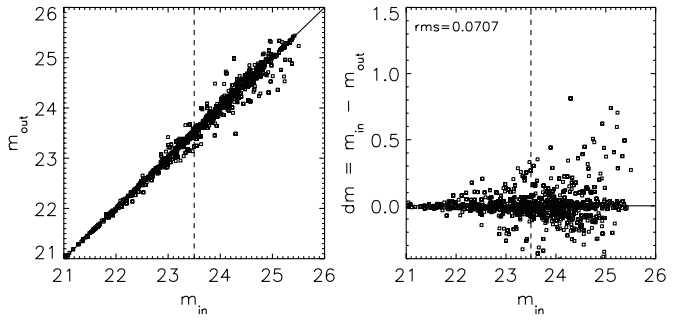

Figure 5. Effect of confusion on photometric results of NUV *GALEX* data. Comparison of magnitudes before (m_{in}) and after placing additional artificial galaxies in the field (m_{out}). For galaxies with $m_{\mathrm{in}} \leqslant 23.5$ (reflecting the selection criteria used for the LBG candidate sample) the change in magnitude is relatively small with a rms for the offset $dm_{\mathrm{rms}} = 0.0707$.

3. PHOTOMETRIC REDSHIFTS

We used seven-band photometry from the two *GALEX* (FUV+NUV) and the five SDSS DR5 (u, g, r, i, z) filter bands for photometric redshifts of our final UV selected sample, applying the algorithm from *hyperz v1.1* (Bolzonella et al. 2000). The variance of Lyα opacity in the intergalactic medium (Massarotti et al. 2001) produces a negligible effect at these redshifts. The redshift determination is done by cross-correlating a set of template spectra to the colors of the sample galaxies. In the current version of *hyperz* we used a set of four template spectra from Bruzual & Charlot (2003), consisting of an elliptical, Sc, Sd galaxy, and starburst. The resulting redshift distributions for the total galaxy and LBG candidate samples are shown in Figure 6.

To get information about the accuracies of our photometric redshifts estimation, we compared the resulting photo-z's of the final galaxy catalog with a subsample of 448 galaxies for which we have spectroscopic redshifts (see Figures 7 and 8). The spectra were observed using the IMACS multi-object spectrograph at the 6.5 m Baade Magellan telescope (K. A. Harris et al. 2009, in preparation). The spectroscopic subsample covers $0.06 < z < 1.34$ with a mean redshift of $\langle z \rangle = 0.48 \pm 0.23$. The photometric redshift accuracy decreases significantly for objects with $m_{\mathrm{NUV}} > 23.5$ mag (Figure 7), and the standard deviation $\sigma_{\Delta z}$ increases from 0.105 (0.129 for LBG candidates) to 0.203 (0.195 for LBG candidates). We therefore restricted our analyses to objects brighter than $m_{\mathrm{NUV}} = 23.5$ (blue and green triangles in Figures 7 and 8). This leaves a more conservatively selected sample of the 462 LBG candidates. For our spectroscopic subsample we derived mean offsets of $\langle \Delta z \rangle = -0.031$ for the whole bright sample (blue + green triangles) and $\langle \Delta z \rangle = 0.023$ for the LBG candidate sample (green triangles). We therefore see no significant systematic offsets. The fraction of catastrophic outliers ($\delta z > 3\sigma$; Figure 8) for bright objects ($m_{\mathrm{NUV}} \leqslant 23.5$) is about 2.6% (5.9% for LBG candidates).

Using our *GALEX* plus seven-band SDSS photometry, we are able to obtain unbiased photometric redshifts with well defined uncertainties for objects with NUV $\leqslant 23.5$ for both the complete galaxy as well as the LBG sample. Hence our LBG selection should be reasonably robust, given the depth in redshift of our four galaxy samples (see Sections 4 and 5) which is 2σ–3σ

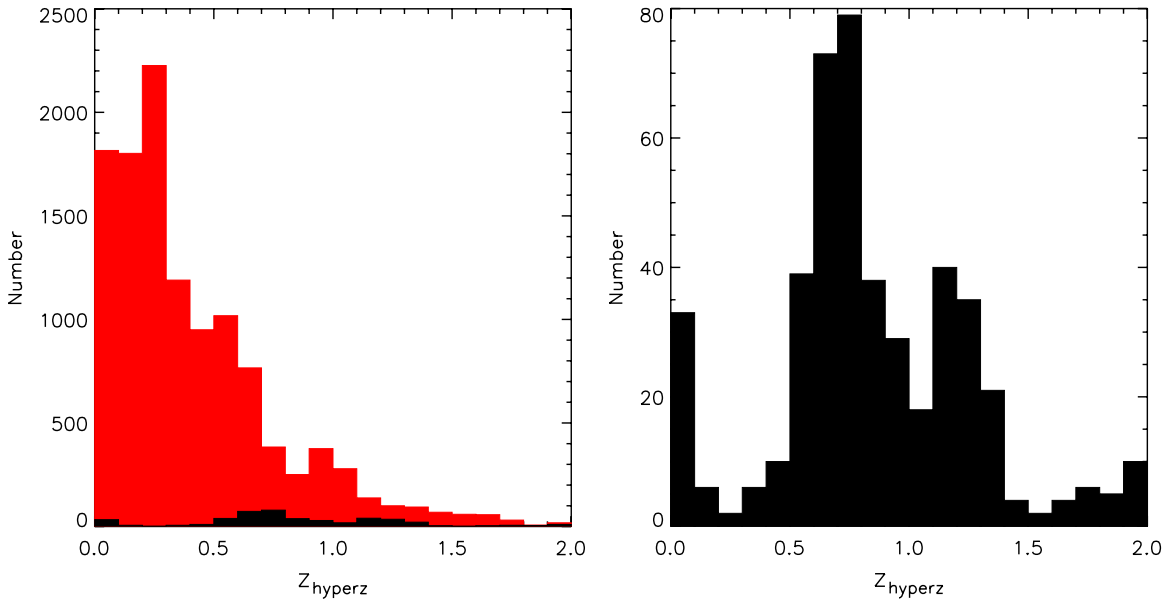

Figure 6. Photometric redshift distribution for all galaxies (left, red) and the LBG candidates (left and right black). We used a bin size for the redshift of $\delta z = 0.1$. The red bars (left panel) represent the distribution in redshift for all galaxies for which we also have SDSS counterparts, while the black filled bars (left+right panel) display the photometric redshift distribution for the LBG candidates.

(A color version of this figure is available in the online journal.)

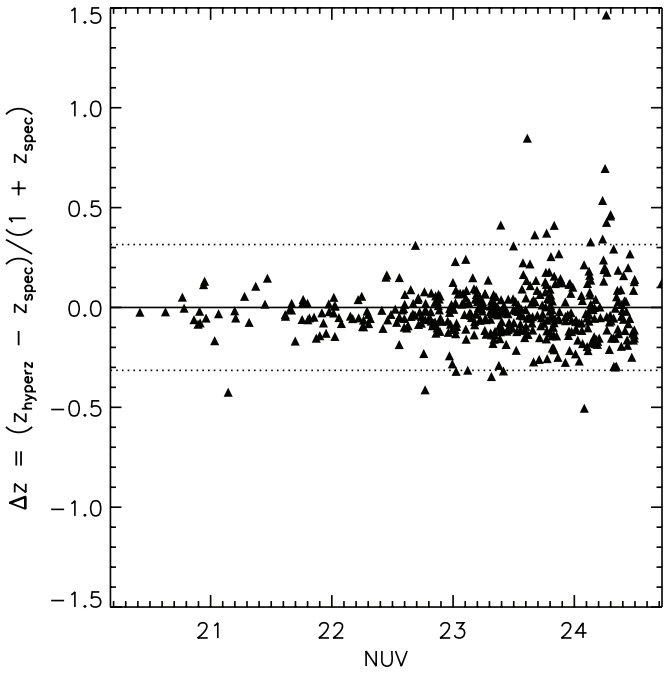

Figure 7. Total NUV magnitude in relation to the photometric redshift accuracy δz. The dashed lines represent the 3σ deviation from the $\delta z = 0$ line. For galaxies fainter than 23.5 mag, the photometric redshift accuracy decreases significantly.

for the derived uncertainties of our photometric redshifts. We therefore assume no significant impact from the relatively large photo-z scatter on our results.

A listing of our LBG sample is in Table 2, available in the electronic edition of this paper. We also provide information on the LBGs on our team Web site.[16]

[16] http://www.physics.uofl.edu/lqg

4. SED FITTING

To constrain the evolution of galaxies in the dense quasar environment of the two LQGs, we compared averaged SEDs built out of the photometric measurements of our sample galaxies to model SEDs derived from the synthesis evolution model PEGASE (Fioc & Rocca-Volmerange 1997). We used a library of several thousand PEGASE spectra from an extended parameter study to probe the star formation histories (SFHs) of a sample of low surface brightness (LSB) galaxies (L. Haberzettl et al. 2009a, in preparation).

We made stacked SEDs of our LBG candidate samples (Section 5) from the *GALEX*+SDSS seven-band photometry. The stacked SEDs were constructed for four different redshift bins over $0.5 \leqslant z < 0.7$ (foreground sample FG1), $0.7 \leqslant z < 0.9$ (LQG0.8), $0.9 \leqslant z < 1.2$ (foreground sample FG2) and $1.2 \leqslant z < 1.5$ (CCLQG). To reduce the influence of extreme objects (e.g., redshift outliers, misidentified stars) we applied upper flux limits for the averaged SEDs in all filter bands, excluding iteratively all objects which have fluxes more than 3σ from the mean flux. Additionally, we only used objects which have non-negative fluxes in all filter bands. The errors for the mean fluxes in the single filter bands are represented by their standard deviations. By fitting the model SEDs to averaged low resolution spectra of our LBG sample, we were then able to obtain SFHs and luminosity-weighted ages (results described in Section 5). The model SED library contains spectra calculated for different star formation laws (SFLaws), SFRs, and extinction geometries. The model SEDs were constructed accounting for consistent chemical evolution. This is a more realistic approach than the use of simple stellar populations (SSPs) with fixed metallicities, giving us the advantage that the metallicity is not a free parameter. Therefore, we preferred PEGASE over other models as for example the widely used Bruzual & Charlot models (Bruzual & Charlot 2003). We chose four different SFLaws including starburst scenarios, constant, exponentially decreasing, and power-law SFRs. The best matching SEDs were derived by performing a χ^2-fit between model and measured

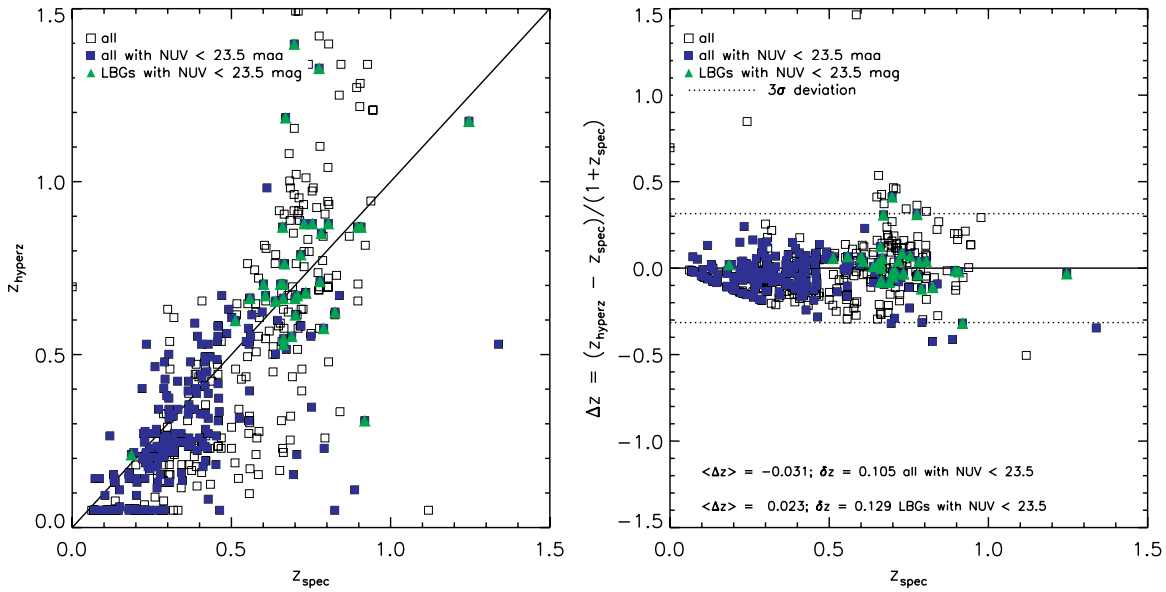

Figure 8. Left panel shows the comparison of our photometric redshifts z_{hyperz} obtained using seven-band photometry (FUV,NUV,u, g, r, i, z) to spectroscopic redshifts which we obtained for a subsample of 448 galaxies. Blue triangles are galaxies with $m_{\rm NUV} \leqslant 23.5$ mag. Green triangles represent the LBG candidates with $m_{\rm NUV} \leqslant 23.5$ mag. The right panel shows the residuals δz using the same color schemes. From the right panel we see that the number of catastrophic outliers is relatively small (all 2.6% and LBG candidates 5.9%) for galaxies with $m_{\rm NUV} \leqslant 23.5$.

(A color version of this figure is available in the online journal.)

SEDs. To judge the quality of our SED fit results we compare the reduced χ^2-values against the ages of the fitted SEDs (Figures 11(a)–(d)[17]), which is the parameter of main interest to us. From these plots we estimate the 1σ uncertainties by comparing χ^2 for every SED to $\chi^2_{\rm min} + 1$.

Since we are analyzing samples of LBG candidates, we set the measured fluxes in the *GALEX* FUV band to zero for those redshift bins where the FUV band would be below 912 Å in the rest frame. We normalized the flux of both modeled and measured SEDs with respect to the rest-frame flux in the z band, and redshift-corrected the measured SEDs according to the mean redshift of the group to which each of the averaged LBG spectra belongs. We next describe the stacked SEDs and results.

5. LYMAN BREAK GALAXY CANDIDATE SAMPLE

Our NUV < 23.5 criterion gives a conservative sample of 462 LBGs, for which our seven-band UV-optical photometric redshift distribution is shown in the two histograms in Figure 6. The red filled bars represent the photometric redshift distribution for the whole galaxy sample, while the LBG candidate sample is represented by the black filled bars. From the right panel we see that most (405) of the LBG candidates have photometric redshifts $z \geqslant 0.5$. The mean photometric redshift of the LBG candidate sample is $\langle z_{\rm LBG} \rangle = 0.86 \pm 0.45$, compared to the mean of the final galaxy sample of $\langle z_{\rm galaxies} \rangle = 0.41 \pm 0.35$. Only 60 LBG candidates lie between $1.2 \leqslant z < 1.5$ and are associated with the CCLQG. We mainly probe the foreground LQG (LQG0.8) at $0.7 \leqslant z \leqslant 0.9$ (117 LBG candidates). The FUV dropout technique effectively identified $z \geqslant 0.5$ galaxies: 88% are at $z \geqslant 0.5$.

For further analysis, we have divided the LBG candidate sample into four redshift bins (Table 3): 0.5–0.7 (FG1 sample), 0.7–0.9 (LQG0.8 sample), 0.9–1.2 (FG2 sample), and 1.2–1.5 (CCLQG). For each redshift bin, we selected two subsamples for intrinsically bright and faint LBG candidates according to their absolute brightness in the *GALEX* NUV filter band (rest frame FUV). For the selection we used the values of $M^*_{\rm NUV}$ from Arnouts et al. (2005; $M^*_{\rm NUV} = -19.6$, -19.8, -20.0, and -20.2 from low to high redshift) consistent with the four redshift bins, and K-corrected the measured NUV magnitudes using the *kcorrect* software v4_1_4 of Blanton et al. (2003; see also Figure 9). The bright and faint subsamples consist of 3–69 candidates. For the FG2 and CCLQG sample, we were not able to detect any faint ($M^*_{\rm NUV} \geqslant -19.8$ mag or -19.6 mag) LBG candidates.

Finally, we divided our LBG candidate sample into red and blue subsamples using the MSL in the $g - i$ versus $r - i$ color–color diagram. For all redshift bins, this selection resulted in a larger red than blue subsample and is a first indication that our LBG samples are dominated by either dusty or more evolved galaxies.

5.1. Star Formation History

We used the SED fits of Section 4 (Figures 10(a)–(d)[18]) to constrain the LBG candidate SFHs. Although χ^2-fits did not result in unique solutions (see Figures 11(a)–(d)) the best-fitting SEDs give luminosity-weighted ages between 3.5–6 Gyr for the dust-free models and 1.0–4.0 Gyr for models including dust. Results for the SED fitting are summarized in Tables 4–7 and explained in more detail below.

The best-fitting SFH for the FG1 sample, consisting of 64 LBG candidates with $-20.38 \leqslant M_{\rm NUV} \leqslant -18.85$, is described by an exponentially decreasing SFR (decay time $\tau = 0.5$ Gyr) after 6 Gyr for the dust-free and a starburst after 2.5 Gyr for dust-containing models using an edge-on disk geometry. Subdividing FG1 into a bright ($M_{\rm NUV} < -19.6$) and faint ($M_{\rm NUV} \geqslant -19.6$) subsample resulted in the same SFHs for the dust-free model. For the models including dust the bright subsample is best represented by a 4.0 Gyr old exponentially decreasing SFR

[17] Figures 11(b), (c), and (d) are available in the online version of the paper.

[18] Figures 10(b), (c), and (d) are available in the online version of the paper.

Table 2
Examples for LBG Candidates

Id (1)	R.A.(J2000) (2)	Decl.(J2000) (3)	FUV (4)	ΔFUV (5)	NUV (6)	ΔNUV (7)	u (8)	Δu (9)	g (10)	Δg (11)	r (12)	Δr (13)	i (14)	Δi (15)	z (16)	Δz (17)	z (18)	Δz (19)
LQG_J104745+45136	10:47:45.93	4:51:36.82	25.601	0.855	23.391	0.035	21.880	0.240	21.409	0.061	20.294	0.032	19.807	0.031	19.520	0.104	0.576	0.034
LQG_J104832+45217	10:48:32.36	4:52:17.21	25.732	1.173	23.064	0.032	22.197	0.330	22.282	0.137	21.765	0.126	21.230	0.114	20.961	0.397	0.663	0.220
LQG_J104808+45223	10:48:08.49	4:52:23.37	99.000	99.000	23.314	0.033	22.776	0.446	22.416	0.123	22.119	0.128	21.479	0.106	20.846	0.269	1.154	0.285
LQG_J104710+45329	10:47:10.68	4:53:29.16	25.419	0.779	23.382	0.037	22.420	0.287	22.588	0.121	22.060	0.102	21.911	0.125	21.632	0.428	0.348	0.262
LQG_J104726+45345	10:47:26.29	4:53:45.69	23.411	0.249	20.791	0.007	18.902	0.021	17.756	0.006	17.321	0.005	17.265	0.006	17.222	0.014	0.098	0.015
LQG_J104850+45451	10:48:50.52	4:54:51.50	22.527	0.132	19.450	0.002	15.523	0.009	15.270	0.012	14.503	0.010	11.138	0.001	11.324	0.002	0.851	0.008
LQG_J104656+45529	10:46:56.13	4:55:29.04	22.913	0.184	18.293	0.001	15.433	0.010	11.975	0.001	14.659	0.011	11.102	0.000	13.599	0.016	1.196	0.047
LQG_J104718+45617	10:47:18.30	4:56:17.15	24.271	0.390	20.171	0.003	16.387	0.006	15.045	0.003	14.554	0.004	17.364	0.017	14.330	0.004	1.929	0.004
LQG_J104829+45618	10:48:29.77	4:56:18.67	31.161	180.875	23.206	0.037	22.094	0.782	22.418	0.398	21.160	0.191	19.959	0.096	19.977	0.443	0.798	0.098
LQG_J104735+45712	10:47:35.17	4:57:12.04	25.674	0.956	23.360	0.036	24.247	1.215	22.643	0.159	22.091	0.134	21.638	0.134	20.858	0.289	1.021	0.427
LQG_J104754+45745	10:47:54.93	4:57:45.61	23.499	0.211	20.416	0.004	16.573	0.006	15.109	0.004	14.609	0.004	14.882	0.003	14.420	0.005	0.055	0.032
LQG_J104754+45804	10:47:54.08	4:58:04.16	24.854	0.534	22.771	0.025	22.448	0.428	21.809	0.093	20.712	0.052	20.413	0.057	20.380	0.241	0.416	0.090
LQG_J104851+45808	10:48:51.81	4:58:08.03	24.400	0.498	20.785	0.006	16.396	0.006	14.694	0.004	14.067	0.004	14.119	0.001	13.726	0.004	0.050	0.029
LQG_J104738+45837	10:47:38.29	4:58:37.40	25.209	0.710	23.183	0.034	24.097	1.460	22.021	0.113	21.498	0.109	20.933	0.091	20.573	0.297	0.647	0.106
LQG_J104839+45850	10:48:39.31	4:58:50.02	25.045	0.519	22.835	0.021	22.360	0.282	22.253	0.097	21.842	0.094	21.614	0.112	21.025	0.285	0.553	0.198

Notes. Summary of LBG properties. Column 2: R.A. in hh:mm:ss.ss; Column 3 DEC in +dd:mm:ss.ss; Column 4–17: magnitudes and errors of our seven-band photometry; Column 18+19: photometric redshifts and errors derived using Hyperz.
(This table is available in its entirety in a machine-readable form in the online journal. A portion is shown here for guidance regarding its form and content.)

Table 3
Summary of Selected Subsamples

Name (1)	z (2)	Size (3)	FUV (4)	NUV (5)	u (6)	g (7)	r (8)	i (9)	z (10)	FUV-NUV (11)	$u-g$ (12)	$g-r$ (13)	$i-z$ (14)
FG1	$0.5 \leqslant z < 0.7$	64	25.72 ± 0.60	23.22 ± 0.23	22.89 ± 0.52	22.28 ± 0.35	21.54 ± 0.48	21.07 ± 0.58	20.84 ± 0.68	2.50	0.61	0.74	0.23
LQG0.8	$0.7 \leqslant z < 0.9$	73	25.97 ± 1.07	23.08 ± 0.29	22.69 ± 0.60	22.27 ± 0.45	21.77 ± 0.59	21.05 ± 0.55	20.90 ± 0.76	2.90	0.42	0.50	0.15
FG2	$0.9 \leqslant z < 1.2$	35	25.94 ± 0.78	23.08 ± 0.42	22.40 ± 0.68	22.04 ± 0.47	21.80 ± 0.51	21.45 ± 0.57	21.08 ± 0.50	2.86	0.35	0.25	0.38
CCLQG	$1.2 \leqslant z < 1.5$	25	26.16 ± 1.75	22.07 ± 1.27	19.48 ± 2.70	18.86 ± 3.25	18.72 ± 3.34	18.54 ± 3.25	17.83 ± 3.42	4.08	0.63	0.14	0.72

Notes. The subsamples are selected for the two foreground regions (FG1+FG2) and in the LQGs (LQG0.8+CCLQG). Column 2 gives the redshift interval over which the subsamples were averaged. Columns 4–10 present the averaged total magnitudes in the FUV+NUV and five SDSS filter bands and Columns 11–14 summarize the averaged colors for the four subsamples.

Table 4
SED Fitting Results for Bright-faint Subsamples

Name	Redshift	Bright		Faint		All	
	z	Best (Gyr)	SFLaw	Best (Gyr)	SFLaw	Best (Gyr)	SFLaw
(1)	(2)	(3)	(4)	(5)	(6)	(7)	(8)
FG1	$0.5 \leqslant z < 0.7$	6.0	Expo. decr.	6.0	Constant	6.0	Expo. decr.
LGQ0.8	$0.7 \leqslant z < 0.9$	3.5	Expo. decr.	6.0	Constant	3.5	Expo. decr.
FG2	$0.9 \leqslant z < 1.2$	6.0	Constant	...	...	6.0	Constant
CCLQG	$1.2 \leqslant z < 1.5$	6.0	Constant	...	...	6.0	Constant

Notes. Results for the SED fits of the LBG subsamples in the individual redshift bins using PEGASE models without extinction by dust. The table is split into three blocks for the results of the bright (Columns 3+4), faint (Columns 5+6) LBG subsample as well as the results for the complete LBG candidate sample (Columns 7+8). Every block consists of one column for the age and the SFLaw of the best-fitting model. The redshift bin is indicated in Column 2.

(decay time $\tau = 1.0$ Gyr) assuming a face-on disk geometry for the dust distribution. The faint subsample is best described by a starburst scenario after 2.5 Gyr using an edge-on disk geometry. The dust-free and dusty models for the complete sample and the dust-free models for the bright and faint subsamples are both relatively well constrained, allowing for only one solution within the $\chi^2 + 1$ limit. The ages derived from the dusty models for the bright subsample range between 2.5 and 6 Gyr for a starburst and exponentially decreasing SFRs with different dust geometries. The faint subsample is fitted with 2.5 Gyr old starbursts with spherical, face-on and edge-on dust geometries.

The fits for the FG2 sample ($0.9 \leqslant z < 1.2$) resulted in SFHs with slightly younger luminosity-weighted ages. The total sample included in the fits consists of 35 LBG candidates with $-22.28 \leqslant M_{\rm NUV} \leqslant -20.38$ and could be best fitted by a constant SFR after 6.0 Gyr for the dust-free (only fit acceptable) and a burst scenario after 1.0 Gyr for the dusty model. The dust is assumed to be distributed with a face-on disk geometry. For this redshift slice we were not able to detect a faint subsample. The acceptable SEDs including dust result in starbursts with ages ranging between 1 to 1.4 Gyr using the five different dust geometries in the library (spherical, inclination averaged, face-on, 45° inclined, and edge-on).

The foreground LQG (LQG0.8 sample) consists of 73 LBG candidates with absolute magnitudes $-20.97 \leqslant M_{\rm NUV} \leqslant -19.67$. The SFH is best described by an exponentially decreasing SFR (decay time $\tau = 0.5$ Gyr) after 3.5 Gyr for the dust-free and a starburst after 1.4 Gyr for the dusty models (edge-on disk). For the bright ($M_{\rm NUV} < -19.8$) and faint ($M_{\rm NUV} \geqslant -19.8$) subsamples the SFHs were best fitted by exponentially decreasing SFRs (decay time $\tau = 0.5$ Gyr) after 3.5 Gyr (bright) and constant SFR after 6 Gyr (faint) assuming dust-free models. The models including dust extinction were best fitted by a starburst after 1.4 Gyr (bright) and an exponentially decreasing SFR (faint, decay time $\tau = 0.5$ Gyr) after 3.5 Gyr, respectively. The dust distributions are assumed to represent edge-on (bright) and 45° inclined disk (faint) geometries. The dust-free models for the complete, bright, and faint subsamples are well constrained, allowing for one fit within the 1σ limit. For the models including dust, the acceptable fits result in ages between 1.2 and 3 Gyr for the complete and 1.2 and 6 Gyr for the faint subsample using a starburst for the complete and an exponentially decreasing SFR for the faint subsample including all dust geometries. The bright subsample is well represented by exponentially decreasing SFR after 3.5 Gyr using an inclination averaged or 45° disk dust geometry.

The CCLQG LBG sample only consists of 25 LBG candidates with absolute magnitudes $M_{\rm NUV} \geqslant -21.34$. Therefore, we could only derive SFHs for the $M > M^*$ LBG candidates. For dust-free models, the SFH is best described by a constant SFR after 6 Gyr (only acceptable solution), while for the models including extinction the best fit is from a starburst after 3 Gyr (spherical dust geometry). The dusty models also allow for solutions ranging from 1.6 to 4 Gyr for the age, using starbursts with all five possible dust geometries.

The SFHs for all subsamples resulted in significantly older best-fitting ages compared to the results of Burgarella et al. (2007). The ages derived here correspond to formation redshifts between 1.5 and 5, which is consistent with the peak of the luminosity density in the universe (e.g., Nagamine et al. 2000; Sawicki & Thompson 2006). Although we have no direct measurement of the dust content for our LBG candidates, the dusty models fit best the LBG candidate samples in the two LQGs (LQG0.8 and CCLQG), indicating that dust plays a non-negligible role.

The relatively large red to blue subsample sizes and the old ages for the LBG candidate samples indicate that the populations are dominated by evolved redder galaxies in comparison to the LBG sample of Burgarella et al. (2007). The best-fitting model SEDs give mean luminosity-weighted ages between 1.2 and 6 Gyr[19], with similar results for blue and red subsamples. Dusty model estimates range over 1.0–5 Gyr. The acceptable range of SED fits for the models including dust allows for ages as young as 0.9 Gyr.

5.2. Luminosity Function

We estimated the LFs for our LBG candidate samples in the four different redshift bins using $1/V_{\rm max}$ (Schmidt 1968) We used k-corrected NUV magnitudes to estimate rest frame FUV fluxes, covered by the *GALEX* NUV filter band at our redshift intervals.

For the $1/V_{\rm max}$ method, we followed the approach used by many other studies (e.g., Eales 1993; Lilly et al. 1995; Ellis et al. 1996; Arnouts et al. 2005; Willmer et al. 2006)

$$\Phi(M, z) = \sum_{i=1}^{N} \frac{\omega_i}{V_{{\rm max},i}\,\Delta m} \tag{2}$$

where ω_i represents the weighting factor accounting for incompleteness. The maximum volume a galaxy can be observed and still satisfy the sample selection criteria is described by (Hogg 1999)

$$V_{\rm max} = \left(\frac{c}{H_0}\right)^3 d\Omega \left(\int_{z_l}^{z_u} \frac{dz}{\sqrt{\Omega_m (1+z)^3 + \Omega_\Lambda}}\right)^3 \tag{3}$$

For the integration limits we used the fixed limits z_l,z_u of our four different redshift intervals. We calculated the errors for the LF using

$$\sigma_\Phi(M, z) = \sqrt{\sum_{i=1}^{n} \left(\frac{\omega_i}{V_{{\rm max},i}\,\Delta m}\right)^2}. \tag{4}$$

The results are compared to parameterizations of the Schechter function as derived by Arnouts et al. (2005; see Figure 12). For

[19] Figures 10(c), (d), and 11(c), (d) are available in the online version of the paper.

Table 5
SED Fitting Results for Bright-faint Subsamples Including Extinction

Name	Redshift	Bright			Faint			All		
	z	Best (Gyr)	SFLaw	Dust geometry	Best	SFLaw (Gyr)	Dust geometry	Best	SFLaw	Dust geometry
(1)	(2)	(3)	(4)	(5)	(6)	(7)	(8)	(9)	(10)	(11)
FG1	$0.5 \leqslant z < 0.7$	4.0	Expo. decr.	Face-on disk	2.5	Burst	Spherical	2.5	Burst	Edge-on disk
LGQ0.8	$0.7 \leqslant z < 0.9$	1.4	Burst	Edge-on disk	3.5	Expo. decr.	45° incl. disk	1.4	Burst	Edge-on disk
FG2	$0.9 \leqslant z < 1.2$	1.0	Burst	Face-on disk	...	...	...	1.0	Burst	Face-on disk
CCLQG	$1.2 \leqslant z < 1.5$	3.0	Burst	Spherical	...	...	...	3.0	Burst	Spherical

Note. Results for the SED fitting of the LBG subsamples for the individual redshift bins as described in Table 4 except now including extinction due to dust in the PEGASE models.

Table 6
SED Fitting Results for Color Selected LBG Subsamples

Name	Redshift	Blue		Red	
	z	Best (Gyr)	SFLaw	Best (Gyr)	SFLaw
(1)	(2)	(3)	(4)	(5)	(6)
FG1	$0.5 \leqslant z < 0.7$	6.0	Constant	6.0	Constant
LGQ0.8	$0.7 \leqslant z < 0.9$	6.0	Constant	3.5	Expo. decr.
FG2	$0.9 \leqslant z < 1.2$	6.0	Constant	6.0	Constant
CCLQG	$1.2 \leqslant z < 1.5$	6.0	Constant	6.0	Constant

Notes. Results for the SED fitting of the LBG color selected subsamples using models without extinction by dust. The selection was done according to their location in the $g - i$ versus $r - i$ color–color diagram. The MSL has been used to separate the blue and red subsample. The table is split into two blocks for the results of the blue (Columns 3+4), and red (Columns 5+6) LBG subsample. Every block consists of one column for the age and the SFLaw of the best-fitting model. The redshift bin is indicated in Column 2.

the FG1,FG2 and LQG0.8 samples we were able to cover the LF down to roughly M^*. For the CCLQG at $1.2 \leqslant z < 1.5$ we were only able to derive the LF for LBG candidates down to roughly $3M^*$, including only two bright magnitude bins.

The Schechter parameterization derived by Arnouts et al. (2005) for all types of NUV-selected galaxies in Figure 12 is exceeded by the data, which implies that in all four redshift bins the LBGs are over-abundant for their redshift. In the two LQGs at $z \sim 0.8$ and $z \sim 1.3$ the volume densities of the LBGs are consistent with Arnouts et al. parameterization of the LFs at $1.75 < z < 2.25$ or LBGs at $2.5 < z < 3.5$. In comparison to the two foreground samples (FG1 and FG2) we also find an increase in the abundances of LBGs for the two LQGs. Although the uncertainties in photometric redshifts are large and there is some blending with the less dense foreground regions, there is a clear indication for higher densities of star-forming galaxies in the two LQGs from the LFs. We have a sample of 112 LBG candidates for the foreground sample FG1 and 117 for the foreground LQG (LQG0.8). Since the volume decreases by 43% from $0.5 \leqslant z < 0.7$ to $0.7 \leqslant z < 0.9$, we estimate an overdensity of $46\% \pm 7\%$ or 2.6σ for the LQG0.8 compared to the FG1 sample. The overall higher volume densities for LBGs in all four redshift bins may at least partly be due to our LBG selection criteria which include galaxies which are relatively evolved.

5.3. LBG Concentrations and LBG–quasar Correlations

In Figure 13 we show the density maps of LBGs photometrically selected to be at $0.7 < z < 0.9$ (left panel) and $1.2 < z < 1.5$ (right panel). The LBG density maps were computed using a variant of the adaptive kernel method (Silverman 1986) in which each LBG in the redshift slice is represented by

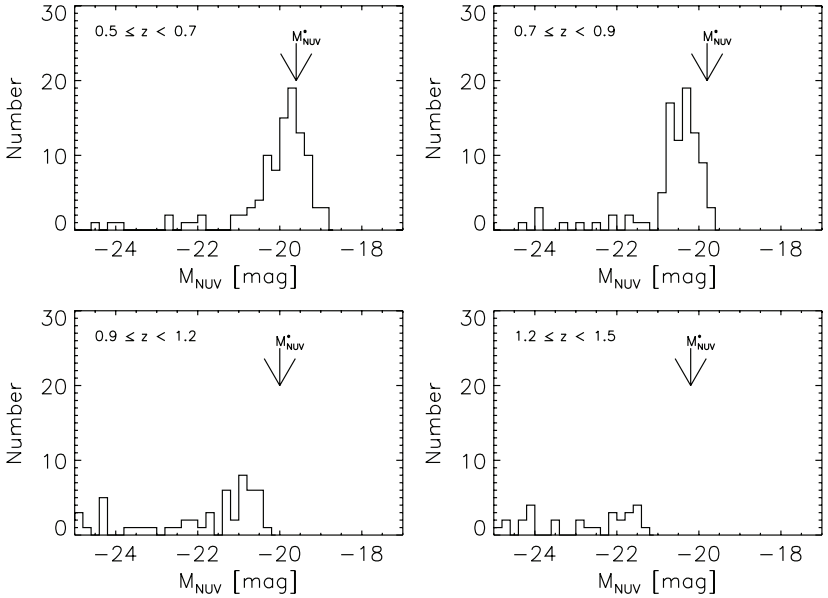

Figure 9. Distribution of absolute NUV magnitudes (rest frame FUV) used to select the bright and faint LBG subsample. The selection limits are indicated by the values for the $M^*_{\rm NUV}$ of Arnouts et al. (2005, $M^*_{\rm NUV} = -19.6, -19.8, -20.0$, and -20.2 from low to high redshift) at the individual redshifts.

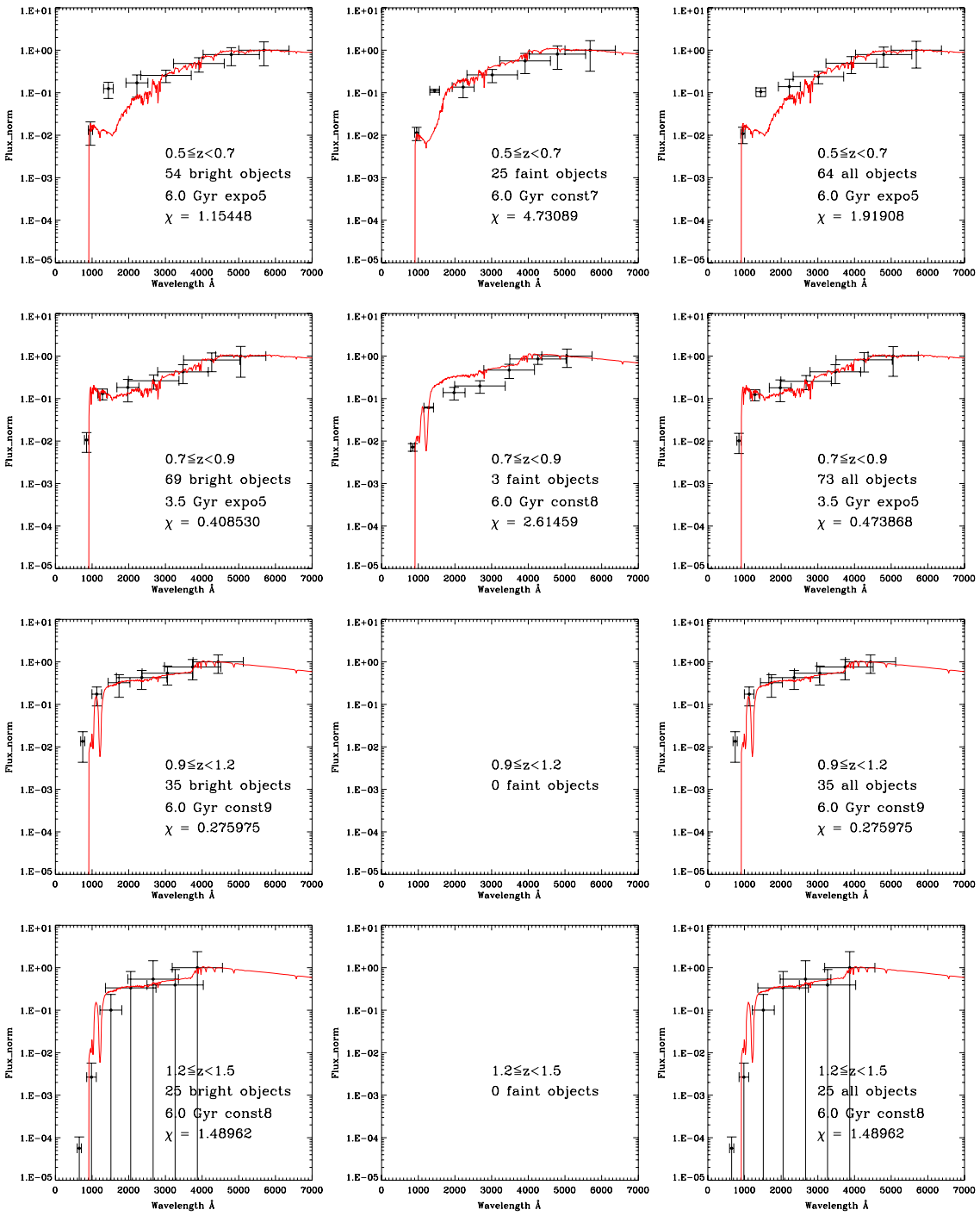

Figure 10. Averaged SED of the LBG candidates (black) found in the *GALEX* data. The LBG candidates are fitted with PEGASE models without dust. The samples are divided into bright (left column) and faint (middle column) subsample. The right column shows the results for the combined sample. We also divided the LBG sample into 4 redshift bins from $z \geqslant 0.5$ (top) to $z < 1.5$ (bottom). The red/light lines represent the best-fitting model SEDs.

(An extended color version of this figure is available in the online journal.)

a Gaussian kernel centered on the LBG. Following Haines et al. (2007), we define the width of the Gaussian kernel to be equal to the distance to the third nearest neighbor LBG within the same redshift slice, and then calculate the local density at each point as the sum of the Gaussian kernels. The isodensity contours in each plot are linearly spaced at intervals of 20 LBGs deg^{-2}, the first contour corresponding to an LBG density of 20 deg^{-2}.

A number of distinct structures appear in the $z \sim 0.8$ LQG. For the CCLQG at $z \sim 1.3$ we were only able to detect the brightest LBG candidates with $L_{\rm NUV} \geqslant 1.5 \times 10^{12}\ L_{\odot}$. Several studies have indicated that at $z < 0.5$–1, quasars avoid both the highest density galaxy regions and the field, instead preferentially populating cluster outskirts (e.g., Söchting et al. 2002, 2004; Kocevski et al. 2008). Such behavior is also suggested in Figure 13.

We can test for quasar–LBG correlations in redshift slices using our photometric redshift estimates, for comparison with higher redshift AGN–LBG correlations from Adelberger & Steidel (2005). The largest number of pairs would arise for $0.7 < z < 0.9$, which contains 17 quasars and 117 LBGs.

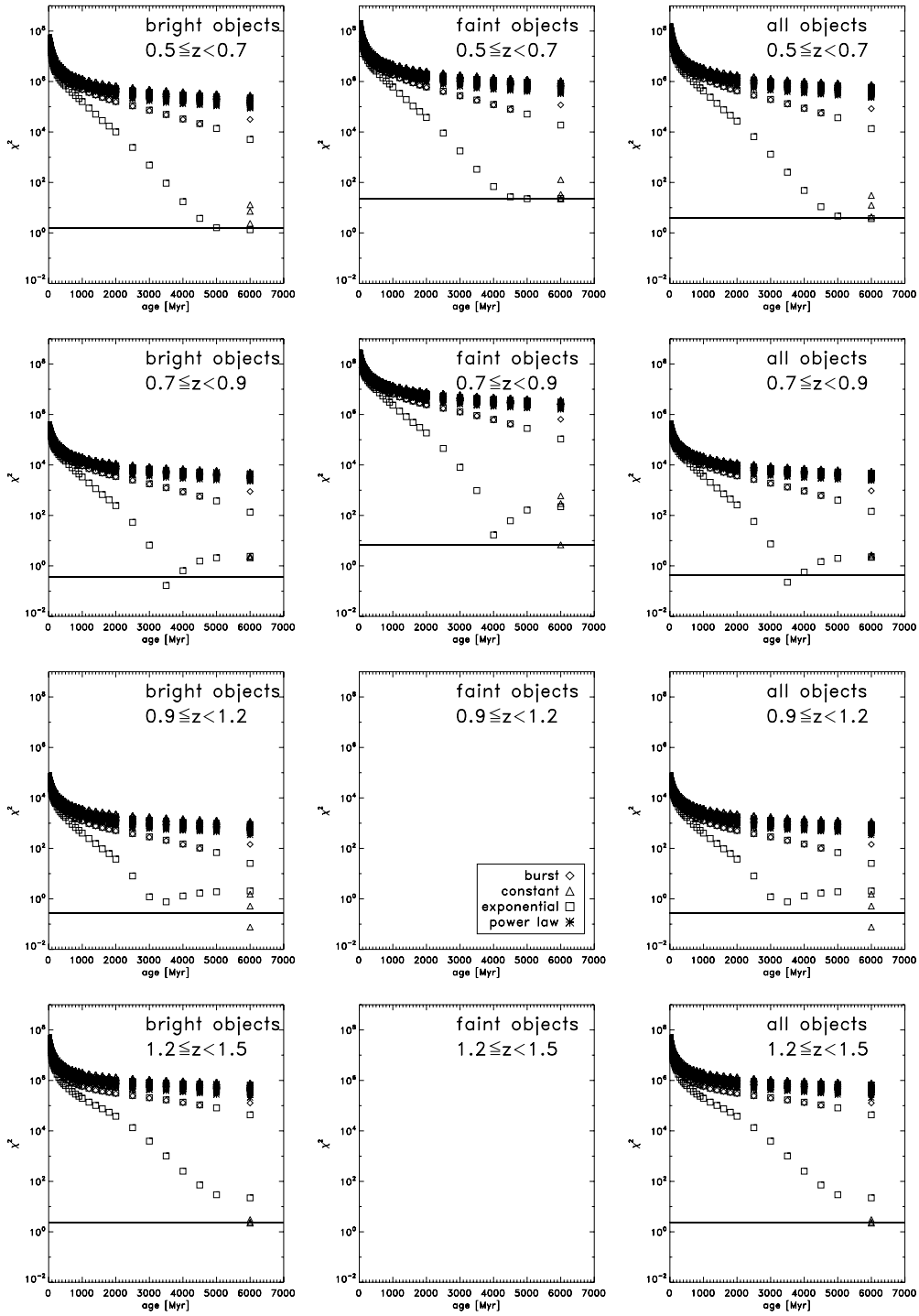

Figure 11. Results of the model fitting (see Figure 10(a)) indicated by the reduced χ^2 vs. age in Myr for bright and faint subsamples as well as the complete galaxy sample according to their redshift intervals. The different symbols indicate fit results for different star formation models used (burst: diamonds; constant: triangles; exponential: squares; power law: asterisks). The horizontal lines represent the 1σ limits in χ^2 for the SED fits.

(An extended color version of this figure is available in the online journal.)

We calculated the nearest neighbor distribution in angular distance in arcminute bins (1 arcmin is 0.8 co-moving Mpc), and compared it with 10,000 randomly placed sets of 17 quasars within the *GALEX* fields. Results indicate mild ($\sim 2\sigma$) overdensities at 2–6 arcmin or ∼1.6–4.8 co-moving Mpc (Figure 14). This is consistent with the LBG–AGN correlation length of Adelberger & Steidel, and a factor of at least 3 smaller than the overdensities around quasars measured by the proximity effect at $2.1 < z < 3.3$ (D'Odorico et al. 2008). Although it could be expected that $z \sim 1$ LBGs would be less massive than their $z \sim 3$ counterparts due to downsizing, our sample appears to be dominated by massive galaxies and could well be similar to the Adelberger & Steidel sample. If quasars have similar regions of enhanced density around them at $z \sim 0.8$ as at $2.1 < z < 3.3$, then $z \sim 0.8$ LBGs would fall in regions of heightened density, but not so high as quasars.

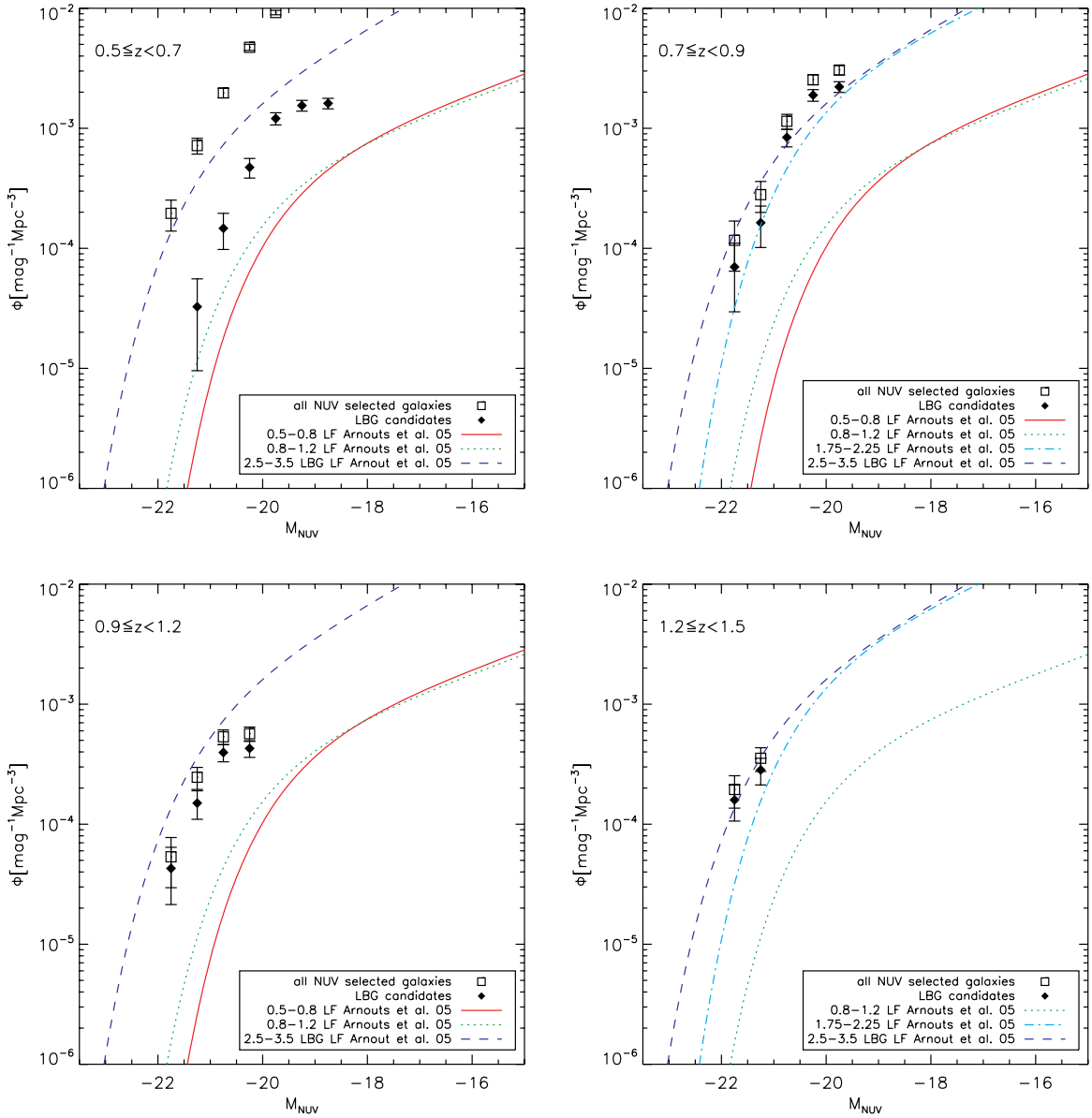

Figure 12. LFs for the LBG candidate samples (filled diamonds) and the all NUV selected galaxies (open squares) in the four different redshift bins. The LFs were derived using the $1/V_{\rm max}$ method. For comparison we plotted LFs for different redshift intervals and selection criteria of Arnouts et al. (2005).

(A color version of this figure is available in the online journal.)

Table 7
SED Fitting Results for Color Selected LBG Subsamples Including Extinction

Name	Redshift	Blue			Red		
	z	Best (Gyr)	SFLaw	Dust geometry	Best (Gyr)	SFLaw	Dust geometry
(1)	(2)	(3)	(4)	(5)	(6)	(7)	(8)
FG1	$0.5 \leqslant z < 0.7$	3.5	Burst	Face-on disk	2.5	Burst	Face-on disk
LGQ0.8	$0.7 \leqslant z < 0.9$	5.0	Burst	Face-on disk	1.4	Burst	Face-on
FG2	$0.9 \leqslant z < 1.2$	1.0	Burst	Spherical	1.2	Burst	Spherical
CCLQG	$1.2 \leqslant z < 1.5$	3.0	Burst	Spherical	2.5	Burst	Spherical

Note. Results for the SED fitting of the LBG subsamples as described in Table 6 now including extinction due to dust in the model SEDs.

6. SUMMARY AND CONCLUSIONS

We present first results from the CCLQG Survey, a 2 deg^2 multiwavelength approach to study one of the largest structures with high quasar density in the high-redshift universe ($z \sim 1$), the CCLQG. The observations also covered a second LQG in front of the CCLQG at $z \sim 0.8$. Our data set includes *GALEX* FUV+NUV images covering a 2 deg^2 field and optical photometry of the NUV selected sample from the SDSS DR5. With *GALEX* data, we reached a detection efficiency rang-

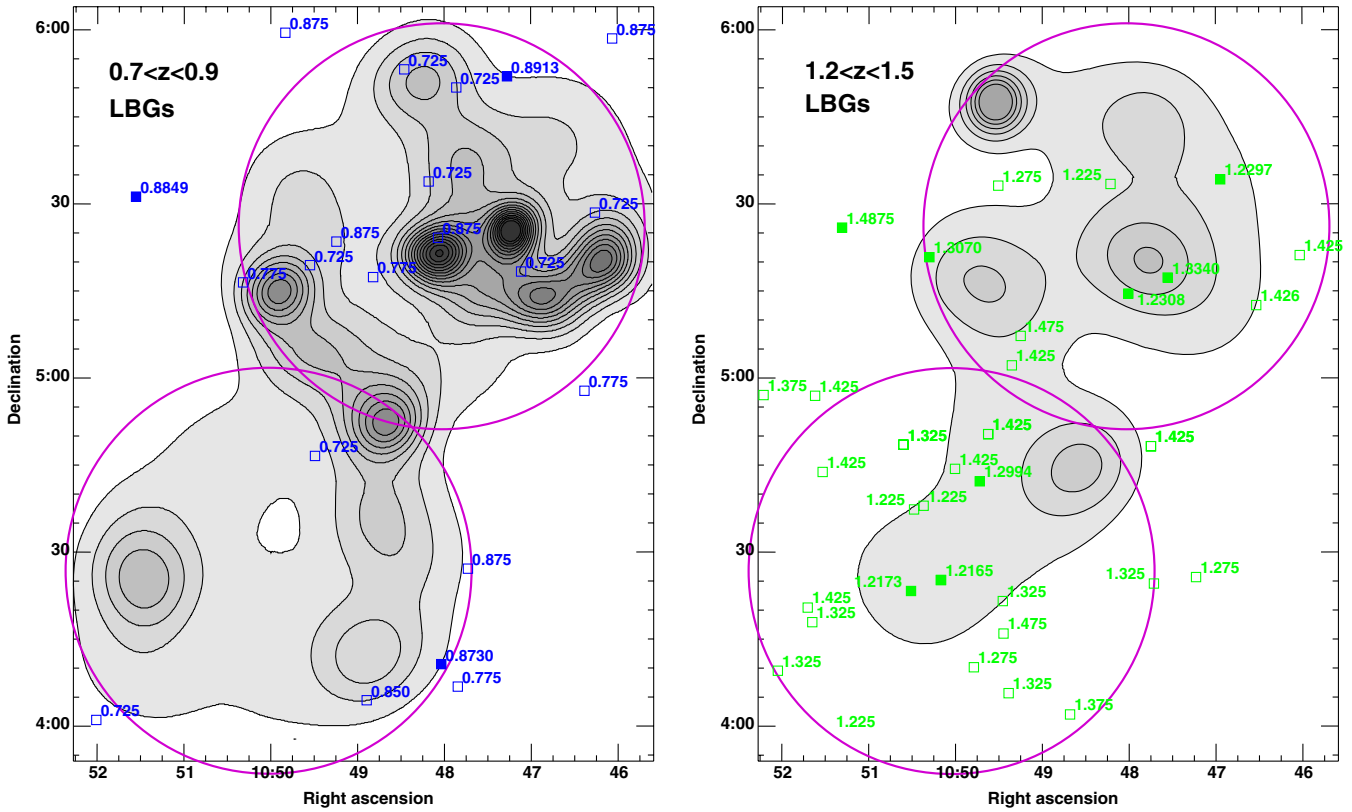

Figure 13. Density plot for the LBGs in the two LQGs at $z \sim 0.8$ (left with blue/dark quasar labels) and $z \sim 1.3$ (right with green/light quasar labels). Filled squares represent spectroscopic and open photometric quasar samples. The two *GALEX* pointings are indicated by the large circles. The lowest density contour represents a density of 20 LBGs deg^{-2} with a separation of 20 LBGs deg^{-2} between contours. Both LQGs show concentrations and structures of LBGs (center of the northern and southeast in the southern *GALEX* field).

(A color version of this figure is available in the online journal.)

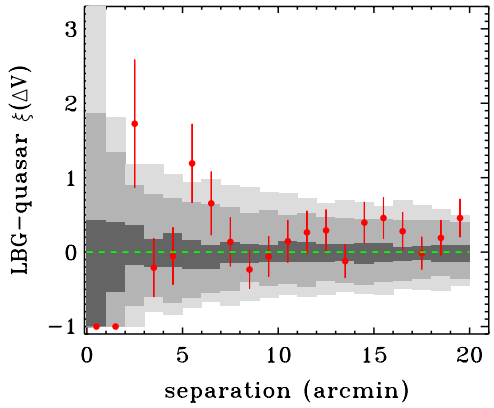

Figure 14. Two point correlation function for LBGs (117) and quasars (17) at $0.7 < z < 0.9$, within the two *GALEX* fields. This redshift slice provides the largest combination of LBG–quasar pairs. Shaded regions denote 68, 95, 99% confidence limits from 10,000 Monte Carlo simulations of sets of 17 random quasar R.A. and Decl. placements in the observed area. Error bars show example 1σ Poissonian errors. At $z = 0.8$, 1 arcmin corresponds to 0.45 local-frame or 0.81 co-moving Mpc. There are no LBG–quasar pairs within 2 arcmin of each other. The signal at 2–3 arcmin arises from 10 pairs. None of the 10,000 simulations had more than 9 in that bin, and we estimate the significance at 3.3σ. The signal at 5–6 arcmin arises from 17 pairs. None of the 10,000 simulations had more than 15 in that bin, and we estimate the significance at 3.1σ. However, the $\sim 1.8\sigma$ overdensity at 6–7 arcmin separation, and the lack of an overdensity at 3–4 arcmin, implies that the overdensity at separation 5–7 arcmin is more robust.

(A color version of this figure is available in the online journal.)

ing between 80%–90%. The detection efficiency declines at $m_{\mathrm{FUV,NUV}} = 24$ due to confusion and incompleteness. Using the FUV-dropout technique, selection criteria adopted from Burgarella et al. (2006) and object classification from SDSS DR5, we were able to select a sample of 1263 star-forming LBG candidates down to $m_{\mathrm{NUV}} = 24.5$. Since photometric redshift uncertainties increase significantly for galaxies with $m_{\mathrm{NUV}} \geqslant 23.5$, we restricted further analysis to a subsample of 462 LBG candidates with $m_{\mathrm{NUV}} \leqslant 23.5$. We derived seven-band photometric redshifts with accuracies $\sigma_{\Delta z} = 0.105$ for all galaxies with $m_{\mathrm{NUV}} < 23.5$ and $\sigma_{\Delta z_{\mathrm{LBG}}} = 0.129$ for the corresponding LBG candidates. The mean photometric redshift of the LBG candidate sample is $\langle z \rangle = 0.86 \pm 0.45$, and the majority of LBGs are at $z < 1$, so we mainly probe the foreground LQG. We derived SFHs for bright and faint LBG candidate subsamples, and found relatively old best-fitting luminosity-weighted ages of 1.0–6 Gyr for models with and without dust. Compared to the results of Burgarella et al. (2007), who estimated ages in the range of 250–500 Myr, our best-fitting ages are significantly older. This indicates that our sample is dominated by more evolved, redder (and likely more massive) LBG candidates. Dividing the LBG candidates into blue and red subsamples using the MSL led to a similar conclusion. The best-fitting SEDs for the blue and red subsamples yielded consistent ages ranging between 1.0 and 6 Gyr. Due to the high uncertainties of the SFHs resulting from the use of broadband photometry and the large scatter of the averaged SEDs, it is important not to over-interpret the results for the luminosity-weighted ages. Our sample of LBG candidates includes only the most luminous galaxies which formed stars over a long period, resulting in a significant population of old red stars to counterbalance the young stars which produce the Lyman break. The faint LBGs

in the LQG0.8 subsample show marginally larger luminosity-weighted ages T_L. A possible explanation is lower SFRs in the fainter subsample, which is supported by evidence for a larger red and more evolved population of LBGs in LQG0.8 compared to FG1 and FG2, which are not coincident with LQGs.

Possible effects of different environment densities can be more clearly observed in the LF for the four redshift slices. The LFs for LBG candidates in the two LQGs show an increased volume density of star-forming galaxies compared to results of less dense regions in the CDF-S (Arnouts et al. 2005). The LBG LF in the foreground LQG (LQG0.8) is consistent with their parameterization of the Schechter function corresponding to $1.75 < z < 2.25$. Although we only have two luminosity bins for the CCLQG, it also shows evidence for an overdensity (more consistent with a population at $2.5 < z < 3.5$). Both redshift slices containing LQGs have larger relative overdensities than the two redshift slices which do not contain quasar overdensities. We derived a sample of 112 LBG candidates for the foreground sample at $0.5 \leqslant z < 0.7$ (FG1) and 117 LBG candidates for the foreground LQG (LQG0.8) and although the volume decreases by 43% between those redshift intervals, the number of LBGs stays about the same. This indicates an overdensity in star-forming galaxies of $46\% \pm 7\%$ or 2.6σ compared to the less dense foreground region FG1. This leads to the conclusion that the high densities in both galaxies (e.g., Williger et al. 2002; Haines et al. 2004) and QSOs are coincident with an overdensity of star-forming galaxies due to LBGs and QSOs; both types of objects trace an underlying overdensity of galaxies.

The LBGs in the LQG0.8 redshift slice appear to show substructure in the host LQG, as shown in the density plots in Figure 13. When compared to quasar locations in the same redshift range, the LBGs and quasars show a marginal overdensity on angular scales corresponding to 1.6–4.8 Mpc, such that quasars prefer the outskirts of dense regions rather than the cores. This result, if confirmed, would be consistent with trends seen at $z < 0.4$ (Söchting et al. 2002, 2004), and also qualitatively noted in a $z \sim 0.9$ supercluster (Kocevski et al. 2008, 2009). It also is consistent with the view that gas-rich mergers cause quasar activity, with such mergers preferentially occurring in regions with excess small-scale galaxy overdensities but not in such dense regions that gas stripping has largely taken place (Hopkins et al. 2008, and references therein).

The two LQGs in the area surveyed here can provide uniquely efficient sites for studying a wide variety of environments and for quasar-galaxy relations. Future studies will require IR imagery to determine stellar masses of galaxies and to refine photometric redshifts to $z \sim 1.5$, more spectra to confirm the location and nature of clusters in the field and their relation to the rich quasar environment, deeper UV observations to probe the LBG LF within the $1.2 < z < 1.5$ CCLQG. X-ray observations would be able to confirm virialized regions within the LQGs.

This publication makes use of data from *GALEX* Cycle 1 observations and is supported by NASA grant NNX05GK42G. Chris Hains acknowledges financial support from STFC. We thank David Koo, David Rosario, and Dave Schiminovich for their very useful comments. This paper includes data gathered with 6.5 m Magellan Telescope located at Las Campanas Observatory, Chile.

L.E.C. received partial support from Center of Excellence in Astrophysics and Associated Technologies (PFB 06).

Funding for the Sloan Digital Sky Survey (SDSS) and SDSS-II has been provided by the Alfred P. Sloan Foundation, the Participating Institutions, the National Science Foundation, the U.S. Department of Energy, the National Aeronautics and Space Administration, the Japanese Monbukagakusho, and the Max Planck Society, and the Higher Education Funding Council for England. The SDSS Web site is http://www.sdss.org/.

The SDSS is managed by the Astrophysical Research Consortium (ARC) for the Participating Institutions. The Participating Institutions are the American Museum of Natural History, Astrophysical Institute Potsdam, University of Basel, University of Cambridge, Case Western Reserve University, The University of Chicago, Drexel University, Fermilab, the Institute for Advanced Study, the Japan Participation Group, The Johns Hopkins University, the Joint Institute for Nuclear Astrophysics, the Kavli Institute for Particle Astrophysics and Cosmology, the Korean Scientist Group, the Chinese Academy of Sciences (LAMOST), Los Alamos National Laboratory, the Max-Planck-Institute for Astronomy (MPIA), the Max-Planck-Institute for Astrophysics (MPA), New Mexico State University, Ohio State University, University of Pittsburgh, University of Portsmouth, Princeton University, the United States Naval Observatory, and the University of Washington.

Facilities: GALEX, Sloan, Magellan:Baade(IMACS)

REFERENCES

Adelberger, K. L., & Steidel, C. C. 2005, ApJ, 627, L1
Adelman-McCarthy, J. K., et al. 2006, ApJS, 162, 38
Adelman-McCarthy, J. K., et al. 2007, ApJS, 172, 634
Arnouts, S., et al. 2005, ApJ, 619, L43
Balogh, M. L., et al. 2004, ApJ, 615, L101
Bell, E. F., et al. 2005, ApJ, 625, 23
Bertin, E., & Arnouts, S. 1996, A&AS, 117, 393
Bianchi, L., et al. 2007, ApJS, 173, 659
Blanton, M. R., et al. 2003, AJ, 125, 2348
Bolzonella, M., Miralles, J.-M., & Pelló, R. 2000, A&A, 363, 476
Bruzual, G., & Charlot, S. 2003, MNRAS, 344, 1000
Burgarella, D., et al. 2007, MNRAS, 380, 986
Burgarella, D., et al. 2006, A&A, 450, 69
Cassata, P., et al. 2007, ApJS, 172, 270
Clowes, R. G., & Campusano, L. E. 1991, MNRAS, 249, 218
Clowes, R. G., & Campusano, L. E. 1994, MNRAS, 266, 317
Clowes, R. G., Campusano, L. E., & Graham, M. J. 1999, MNRAS, 309, 48
Coia, D., et al. 2005, A&A, 430, 59
Coil, A. L., Hennawi, J. F., Newman, J. A., Cooper, M. C., & Davis, M. 2007, ApJ, 654, 115
Cooper, M. C., et al. 2007, MNRAS, 376, 1445
Cooper, M. C., et al. 2008, MNRAS, 383, 1058
Covey, K. R., et al. 2007, AJ, 134, 2398
Croom, S. M., et al. 2004, MNRAS, 349, 1397
D'Odorico, V., et al. 2008, MNRAS, 389, 1727
Doroshkevich, A., & Dubrovich, V. 2001, MNRAS, 328, 79
Duc, P.-A., et al. 2002, A&A, 382, 60
Eales, S. 1993, ApJ, 404, 51
Elbaz, D., et al. 2007, A&A, 468, 33
Ellis, R. S., Colless, M., Broadhurst, T., Heyl, J., & Glazebrook, K. 1996, MNRAS, 280, 235
Evrard, A. E., et al. 2002, ApJ, 573, 7
Fioc, M., & Rocca-Volmerange, B. 1997, A&A, 326, 950
Foucaud, S., et al. 2003, A&A, 409, 835
Gerke, B. F., et al. 2007, MNRAS, 376, 1425
Graham, M. J., Clowes, R. G., & Campusano, L. E. 1995, MNRAS, 275, 790
Guillemin, P., & Bergeron, J. 1997, A&A, 328, 499
Haines, C. P., Campusano, L. E., & Clowes, R. G. 2004, A&A, 421, 157
Haines, C. P., Clowes, R. G., Campusano, L. E., & Adamson, A. J. 2001, MNRAS, 323, 688
Haines, C. P., et al. 2007, MNRAS, 381, 7
Hildebrandt, H., et al. 2007, A&A, 462, 865
Hogg, D. W. 1999, arXiv:astro-ph/9905116
Hogg, D. W. 2001, AJ, 121, 1207

Hopkins, P. F., Hernquist, L., Cox, T. J., & Kereš, D. 2008, ApJS, 175, 356
Kocevski, D. D., et al. 2008, arXiv:809.2091
Kocevski, D. D., Lubin, L. M., & Gal, R. 2009, ApJ, 690, 295
Koyama, Y., et al. 2008, MNRAS, 391, 1758
Lilly, S. J., Tresse, L., Hammer, F., Crampton, D., & Le Fevre, O. 1995, ApJ, 455, 108
Madau, P., Pozzetti, L., & Dickinson, M. 1998, ApJ, 498, 106
Marmo, C., & Bertin, E. 2008, in ASP Conf. Ser. 394, Astronomical Data Analysis Software and Systems XVII, ed. R. W. Argyle, P. S. Bunclark, & J. R. Lewis (San Francisco, CA: ASP), 619
Massarotti, M., Iovino, A., Buzzoni, A., & Valls-Gabaud, D. 2001, A&A, 380, 425
Nagamine, K. 2002, ApJ, 564, 73
Nagamine, K., Cen, R., & Ostriker, J. P. 2000, ApJ, 541, 25
Nakata, F., et al. 2002, in Proc. IAU 8th Asian-Pacific Regional Meeting, Vol. II, National Center of Sciences, Hitotsubashi Memorial Hall, Tokyo, July 2–5, ed. S. Ikeuchi, J. Hearnshaw, & T. Hanawa (Tokyo: The Astronomical Society of Japan), 283
Newman, P. R. 1999, Ph.D. thesis, AA, University of Central Lancashire
Noeske, K. G., et al. 2007, ApJ, 660, L43
Papovich, C., Dickinson, M., & Ferguson, H. C. 2001, ApJ, 559, 620
Peng, C. Y., Ho, L. C., Impey, C. D., & Rix, H.-W. 2002, AJ, 124, 266
Pettini, M., et al. 2001, ApJ, 554, 981
Pilipenko, S. V. 2007, Astron. Rep., 51, 820
Porciani, C., & Giavalisco, M. 2002, ApJ, 565, 24
Porter, S. C., Raychaudhury, S., Pimbblet, K. A., & Drinkwater, M. J. 2008, MNRAS, 388, 1152
Postman, M., et al. 2005, ApJ, 623, 721
Quadri, R., et al. 2007, ApJ, 654, 138
Richards, G. T., et al. 2007, BAAS, 38, 994
Sawicki, M., & Thompson, D. 2006, ApJ, 648, 299
Schmidt, M. 1968, ApJ, 151, 393
Schneider, D. P., et al. 2007, AJ, 134, 102
Silverman, B. W. 1986, Density Estimation for Statistics and Data Analysis (Monographs on Statistics and Applied Probability; London: Chapman and Hall)
Söchting, I. K., Clowes, R. G., & Campusano, L. E. 2002, MNRAS, 331, 569
Söchting, I. K., Clowes, R. G., & Campusano, L. E. 2004, MNRAS, 347, 1241
Steidel, C. C., Dickinson, M., Meyer, D. M., Adelberger, K. L., & Sembach, K. R. 1997, ApJ, 480, 568
Steidel, C. C., Giavalisco, M., Pettini, M., Dickinson, M., & Adelberger, K. L. 1996, ApJ, 462, L17
Steidel, C. C., Pettini, M., & Hamilton, D. 1995, AJ, 110, 2519
Swinbank, A. M., et al. 2007, MNRAS, 379, 1343
Teplitz, H. I., et al. 2000, ApJ, 533, L65
Vijh, U. P., Witt, A. N., & Gordon, K. D. 2003, ApJ, 587, 533
Willmer, C. N. A., et al. 2006, ApJ, 647, 853
Wolf, C., et al. 2005, ApJ, 630, 771